NANO-PETROPHYSICS OF THE DEAN, SPRABERRY, AND WOLFCAMP FORMATIONS OF THE MIDLAND BASIN

By

NABIL MZEE

Presented to the Faculty of the Graduate School of
The University of Texas at Arlington in Partial Fulfillment
of the Requirements
For the Degree of

MASTER OF SCIENCE IN GEOLOGY

THE UNIVERISITY OF TEXAS AT ARLINGTON
MAY 2019

ACKNOWLDEGMENTS

I would like to express my sincerest appreciation for the guidance provided by Dr. Max Hu throughout my Masters study. Dr. Hu's commitment and passion for his work is truly an inspiration and I'm very grateful for the immense amount of knowledge I've acquired under his supervision. I would like to thank Dr. Lowell Waite of Pioneer Resources for his efforts with the procurement of my samples and supplementary data as well as Dr. Maijie Fan and Dr. John Wickham for their helpful comments. Thanks also go to Drilling Info for providing a complementary subscription to Dr. Hu's research group.

I would also like to acknowledge Qiming Wang for generously providing his assistance to several members of our research group, including myself, on a voluntary basis. I wish Qiming the best of luck with his future endeavors in his career. Lastly, I would like to thank Ashley, my father, my mother, my sister, and my close friends for their love, support, and many words of encouragement over the last two years. I can't even begin to explain how blessed I am to have people as wonderful as them in my life.

Abstract

NANO-PETROPHYSICS OF THE DEAN, SPRABERRY, AND WOLFCAMP FORMATIONS OF THE MIDLAND BASIN

West Texas, U.S.A

Nabil Mzee, M.S

The University of Texas at Arlington, 2019

Supervising Professor: Qinhong Hu

Technological advances in hydraulic fracturing and horizontal drilling have led to a surge in oil and gas production in unconventional shale reservoirs over the past several decades. The Permian Basin of Northwest Texas and Southeast New Mexico is no exception to this. Since 2009, when the application of these technologies went into full scale, the production in the Permian Basin has more than doubled. Despite the enormous advances in production in the Permian Basin, operators are plagued by rapid decline rates in producing wells. The root cause of the rapid production decline rates is not well understood but there is consensus that the predominance of nanopores in these unconventional reservoirs plays a significant role in the sharp production declines. In order to develop a better understanding of the production behavior in unconventional reservoirs, the nano-petrophysical properties of these reservoirs must be investigated.

This study investigates the nano-petrophysics of the Wolfcamp B, Wolfcamp A, Dean, and Spraberry Formations of the Midland sub-basin in the Permian Basin by Mercury Injection Capillary Pressure (MICP) analysis, spontaneous fluid imbibition tests, vacuum saturation and

liquid displacement tests, x-ray diffraction (XRD), and pyrolysis. Most samples exhibit significant pore size distribution in pore throat diameter ranges associated with intra-clay grain space, organic matter hosted pores, and intragranular pores. Thermal maturation is found to play a significant role in the generation of pores within these pore throat ranges. The hydrophobic pore networks of the samples exhibit a better connectivity than the hydrophilic pore networks of the samples. Lastly, pore size distribution is found to be a significant controlling factor on permeability as the significant presence of pores within the 2.8-50 nm range correlates with lower permeabilities and higher tortuosities in the sample set.

Table of Contents

List of Illustrations

List of Tables

Chapter 1 - Introduction

The Permian Basin is a sedimentary basin located in Northwest Texas and the Southeastern New Mexico and has been a large producer of oil and gas in the past century. Production in the Permian Basin first began in the 1920s and since then, approximately 418,000 wells have been drilled into various conventional and unconventional reservoirs in the basin (Hughes, 2018). Only 146,000 of these wells are still in production today (Hughes, 2018). A recent study by IHS Markit estimates that the Permian Basin still holds an estimated 60 to 70 billion technically recoverable resources (Business Wire, 2017). Production in the Permian Basin reached a peak of 2.2 mbd (million barrels per day) in October of 1973 and had been in slow decline up until 2009 (Hughes, 2018). Since 2009, production in the Permian Basin has more than doubled due to the implementation of hydraulic fracturing and horizontal drilling in unconventional reservoirs. Six formations have been responsible for the significant increase in the Permian Basin's crude oil production, and these formations are the Spraberry, Wolfcamp, Bone Spring, Glorieta, Yeso, and Delaware Formations (EIA, 2014). The afore-mentioned production predominantly (at 70%) has come from the Spraberry, Wolfcamp, and Bone Spring Formations (Hughes, 2018). In addition, 71% of production in the Permian Basin comes from the following seven counties: Eddy, Reeves, Lea, Midland, Loving, Upton, and Reagan Counties (Hughes, 2018). As indicated in Table 1, core samples of the Spraberry, Wolfcamp, and Dean Formations from wells in Martin, Midland, Upton, and Reagan Counties will be used for this study.

Production from the Spraberry, Dean, and Wolfcamp Formations has helped drive the increase in the Permian’s oil production despite declining production from legacy wells of late 20th century. The Spraberry, Dean, and Wolfcamp Formations have been credited for almost

three-quarters of the 60% increase in oil put in the Permian Basin since 2007 (EIA, 2014). The Wolfcamp and Spraberry-Dean plays are some of the largest resource plays in the world and exhibit a great potential to be major suppliers of oil and gas for the next several decades. Despite prolific increases in production since 2009, several wells that target these formations have begun to experience declines in production. Yet, there has been little investigation over the root cause of these production declines (Hu and Ewing, 2014). There are several factors related to fluid migration and pore structure which are believed to contribute to these sharp production declines. This study will further investigate many factors which impact the pore structure and fluid flow in unconventional reservoirs.

Chapter 2 – Geological Setting

2-1 Tectonic Setting and Depositional History

The Permian Basin is a sedimentary basin that covers approximately 86,000 square miles of land in West Texas and the southeastern portion of New Mexico (Ball, 1995). It is primarily composed of two sub-basins, the western Delaware Basin and the eastern Midland Basin, both of which are separated by Central Basin Platform (Figure 2-1).

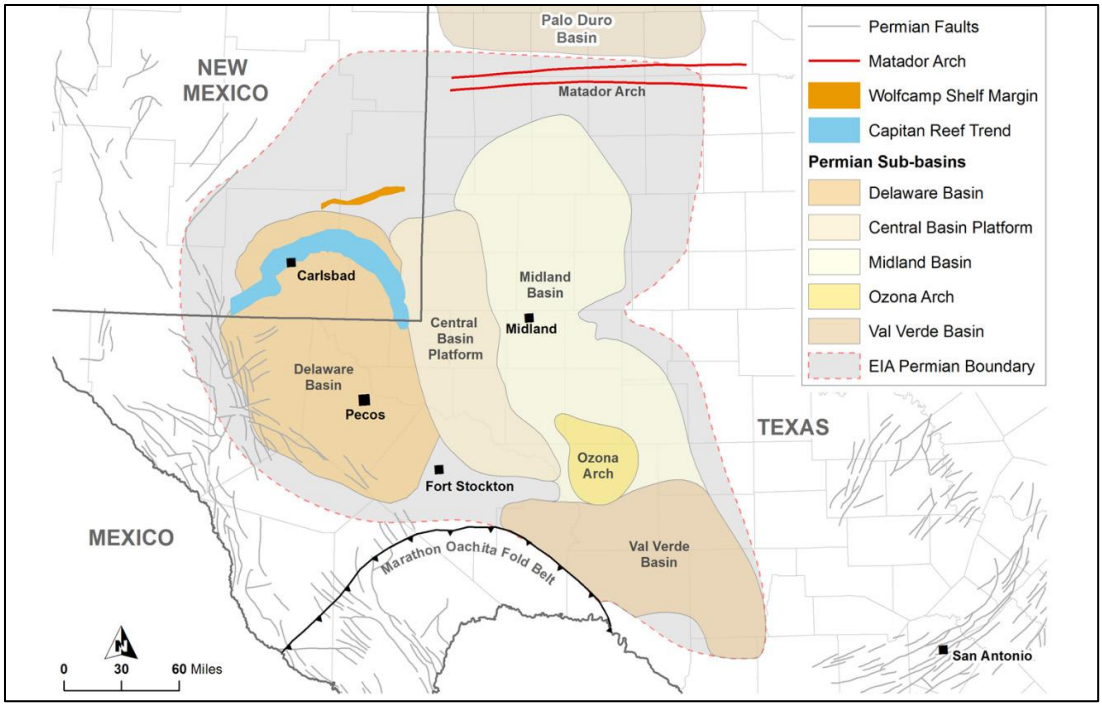

Figure 2-1. Map identifying major tectonic features and areal extent of the Permian Basin (EIA, 2017)

The development of the Permian Basin is distinguished by three stages. The first stage is characterized by the formation of the Tobosa Basin from the Cambrian to the Mississippian. During this time period, the Tobosa basin was a broad marine passive margin characterized by weak crustal extension and low rate subsidence. Deposition between the Cambrian and Mississippian consisted primarily of shallow water carbonates. (SEPM, 2013). However, carbonate deposition during this period was interrupted by shale deposition during the Middle Ordovician, Late Devonian, and Early Mississippian (Hills, 1972). The second stage of the Permian Basin's development was characterized by crustal flexure in the foreland of the Ouachita-Marathon orogenic belt due to the collision of the North American craton and South American craton from the late Mississippian to the Early Permian (Hills, 1984). This crustal flexure reconfigured the ancestral Permian Basin into a sequence of rapidly subsiding sub-basins

disconnected by structural uplifts. One example of this is the Delaware and Midland Basins which were completely separated by Central Basin Platform in the Late Pennsylvanian. During this period, slow black shale deposition occurred in the deep central parts of the basin and broad carbonate reefs developed on the ancestral basin's margins and Diablo and Central Basin Platforms (Hills, 1972). The carbonate reefs of the Central Basin Platform were the main sediment source for the Midland Basin during this time period. The third stage of the Permian Basin's development was characterized by the deposition of vast sedimentary sequences after the basin became structurally stable in the early Permian. Deposition in the early Permian consisted of carbonate materials being deposited on the Permian Basin's Northwestern Shelf, Eastern Shelf, and Central Basin Platform (SEPM, 2013). All the while, finer clastic materials were concurrently settling into the centers of the Delaware and Midland Basins (SEPM, 2013). In the late Guadalupian, there was a transition from carbonate deposition to redbed sandstone in the Northwestern Shelf, Eastern Shelf, Central Basin Platform, and the Midland Basin (SEPM, 2013). Lastly, the sequences were overlain by the evaporite sequences (e.g., halite and anhydrite) of the Ochoan epoch (SEPM, 2013). The lack of tectonic activity after the Permian ultimately played a significant role in the preservation of hydrocarbons in the Permian basin (Soreghan and Soreghan, 2013).

2-2 Stratigraphy of Wolfcamp, Dean, and Spraberry Formations

The entire Permian sequence can exceed 25,000 feet in thickness in certain parts of the Basin (Ball, 1995). In the Midland Basin, the Wolfcampian and Leonardian series includes approximately 2000 to 4500 feet of siliclastic and carbonate rocks that were deposited in deep-water environments (Hamlin, 2012). The Wolfcamp Formation is a constituent of the carbonate sequences that were deposited in the early portion of the Permian period and is distinguished by its Wolfcampian age. Lithology in the Wolfcamp Formation varies from limestone to mixed

limestone and dolomite to shale (Ball, 1995). In the Midland Basin, siliclastic and calcareous mudrock lithofacies dominate the basin center whereas carbonate lithofacies are more common along the sub-basin's margins (Hamlin, 2012). Individual thickness of the Wolfcamp Formation can be measured in tens of feet and occur in intervals approaching 1,000 feet (Ball, 1995). Drilling depths for the Wolfcamp Formation vary from 5,000 to 9,000 feet (Ball, 1995).

The Spraberry and Dean Formations are constituents of the finer clastic sequences that were deposited in the Midland Basin in the early and middle portion of the Permian period. They directly overlie the Wolfcamp Formation and are distinguished by their Leonardian age. The Spraberry and Dean sequences are approximately 150 miles long and 40 to 75 miles wide and are bound on the west by the Central Basin Platform and bound on the east by Eastern Shelf (Ball, 1995). The lithology in the Spraberry and Dean Formations consists of fine-grained sandstone, siltstone, shale, and carbonate (Handford, 1981). Sandstone and siltstone are the predominant types of rock in the Dean and Spraberry Formation. Despite being widely distributed, the sandstones and siltstones of the Dean and Spraberry Formations exhibit little textural and compositional variation and are characterized as quartz-arenite to subarkose (Handford, 1981). Carbonates of the Spraberry and Dean Formations are distinguished by four lithofacies: (1) silty dolomite mudstone; (2) nodular lime wackestone; (3) skeletal grainstone; and (4) lithoclastic rudstone and floatstone (Handford, 1981). Interbedded with sandstone and siltstone, organic-rich shale beds are widely distributed in the Sprayberry and Dean Formations. These organic-rich shale beds are optimal source rocks, containing 1 to 3 percent total organic carbon (Ball, 1995). A generalized stratigraphic column of the Central Basin Platform and Midland Basin is presented in Figure 2.

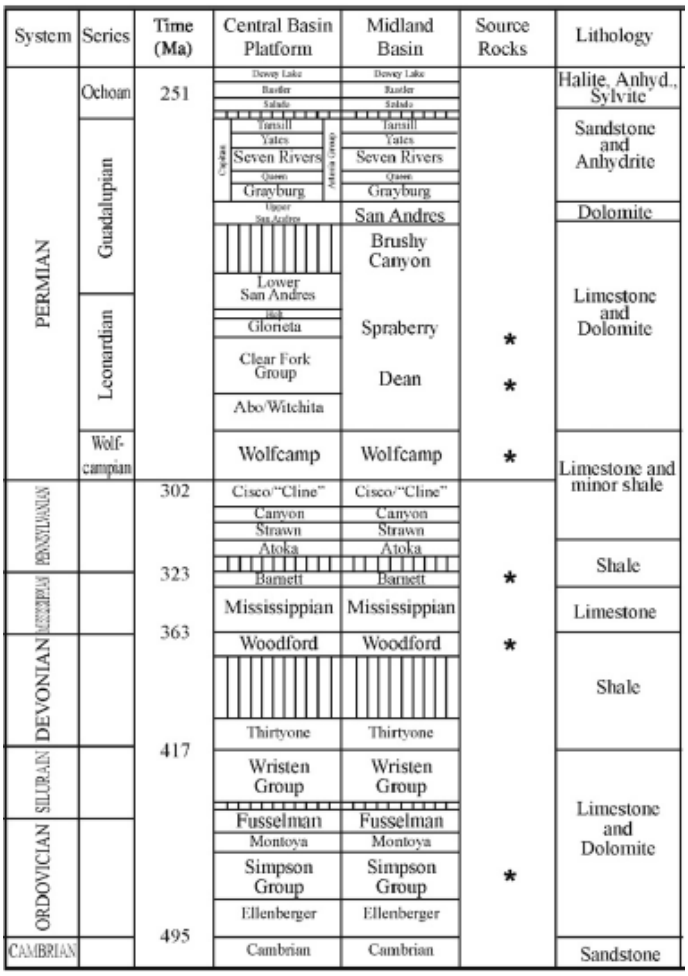

Figure 2-2. Generalized stratigraphy of the Paleozoic Era of the Central Basin Platform and Midland Basin. Star symbology indicates the formation as source rock (from Engle, 2016).

Chapter 3 - Methods

3-1 Sample Procurement

Core samples from 4 wells whose names will remain confidential were provided by Pioneer Natural Resources. The depths of each of the following formations in each well were then identified: Wolfcamp A, Wolfcamp B, Dean, lower Spraberry, middle Spraberry. The provided core samples were then examined, and several sample intervals were collected for each formation. Two core sample intervals were acquired for both the lower and middle Spraberry, four sample

intervals were collected for both Wolfcamp A and Wolfcamp B, and five sample intervals were collected for the Dean Formation. After the intervals from the core samples were collected, a unique sample ID was assigned to each collected sample interval (Table 3-1). Sample IDs were created based on the abbreviation of the formation the interval is from, an abbreviation of the anonymized well name, and the corresponding depth which the sample was collected. The thousands' place digit in the portion of the sample ID which represents the collection depth has been omitted to keep the well identities confidential. Pictures of the samples were captured using a digital camera for whole sample pictures and a microscopic camera for magnified pictures (Figure 3-2). The extent of lamination was recorded based on an arbitrary scale from 1-10; a value of 1 indicates that there is no observed lamination in the sample and a value of 10 indicates that the sample is very laminated. Afterwards, vacuum saturation and fluid displacement test with DI water were performed on the large core samples to determine the effective porosity, bulk density, and grain density. The large core samples were then reduced into smaller sizes and further prepared for various experiments. The large cores were then reduced to 1-cm sided cubes for mercury injection capillary pressure (MICP) analysis, vacuum saturation, liquid displacement, and spontaneous fluid imbibition. These complementary tests were conducted to characterize pore structure, pore connectivity, and fluid interaction within the rock matrix.

Table 3-1: Sample ID of samples used for study

Well Name	Sample ID	Corresponding Formation	Mass (g)
Well W	W537A SPRA	Middle Spraberry	282.7
Well W	W537B SPRA	Middle Spraberry	229.9
Well W	W766 SPRA	Lower Spraberry	412.4
Well W	W767 SPRA	Lower Spraberry	959.2
Well X	X340 WCa	Wolfcamp A	424.6
Well X	X461 WCa	Wolfcamp A	531.9
Well X	X682 WCa	Wolfcamp B	355.4
Well Y	Y538 WCa	Wolfcamp A	396.1
Well Y	Y540 WCa	Wolfcamp A	562.9
Well Y	Y782 WCb	Wolfcamp B	431.7
Well Y	Y863 WCb	Wolfcamp B	411.9
Well Z	Z200 Dean	Dean	305
Well Z	Z201 Dean	Dean	388.7
Well Z	Z279 Dean	Dean	249.3
Well Z	Z281 Dean	Dean	203.3
Well Z	Z293 Dean	Dean	244
Well Z	Z823 WCb	Wolfcamp B	418.65

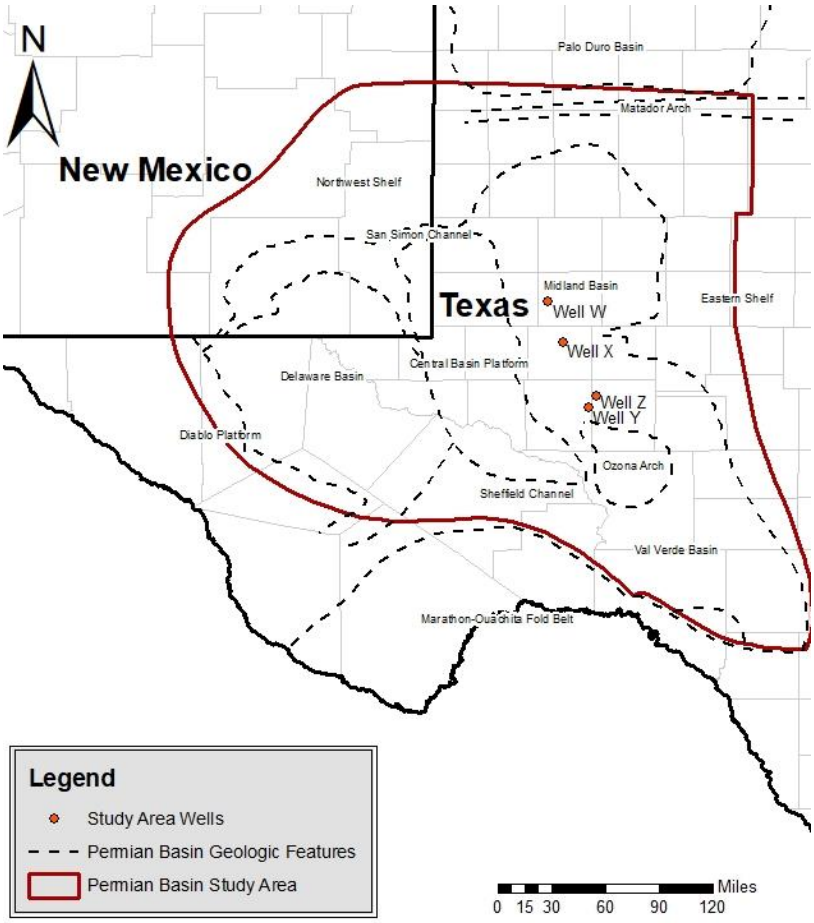

Figure 3-1 Well locations (Bureau of Economic Geology)

A

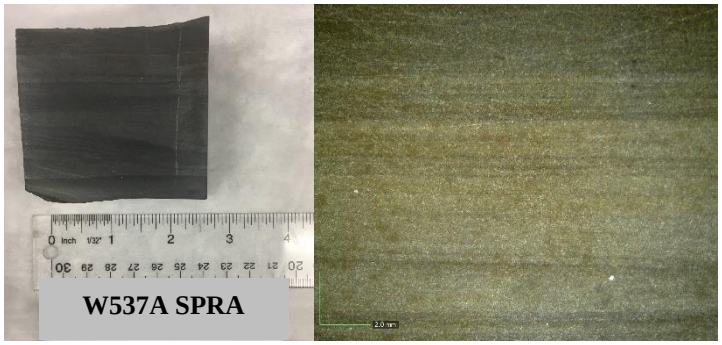

B

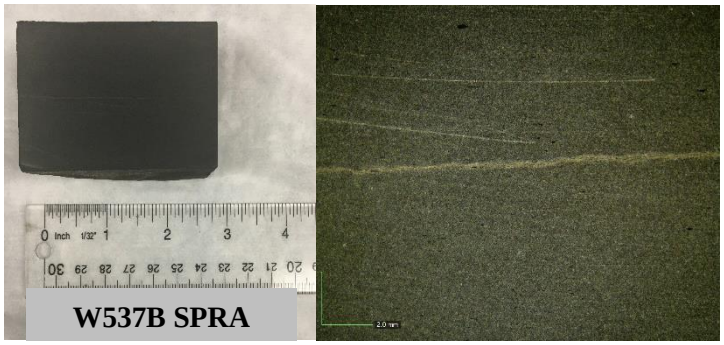

C

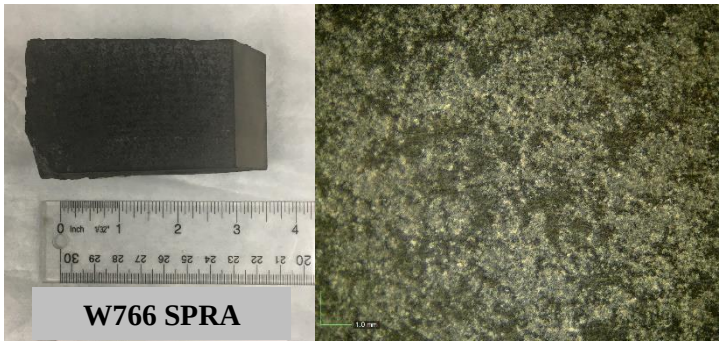

D

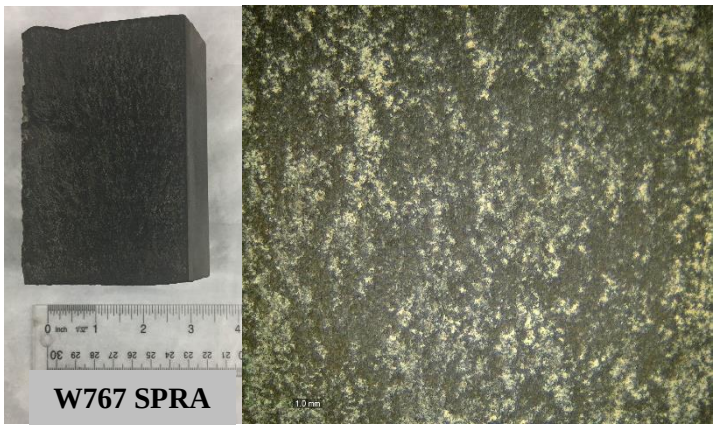

E

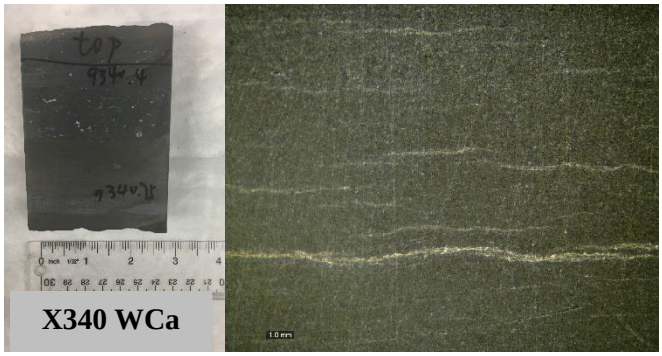

F

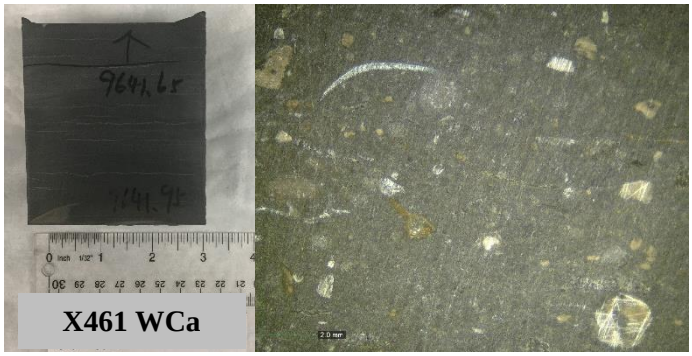

G

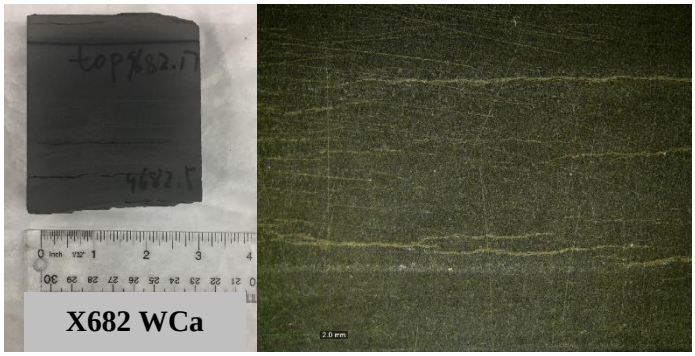

H

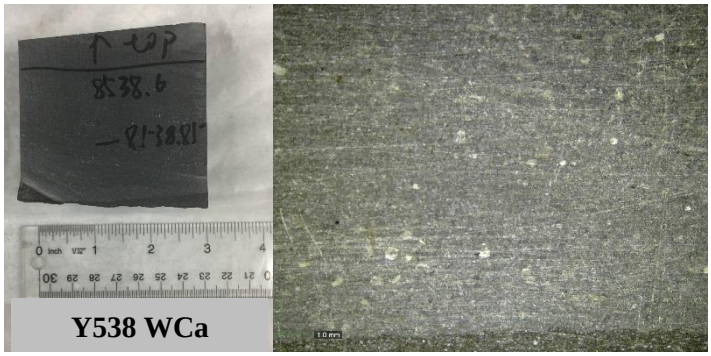

I

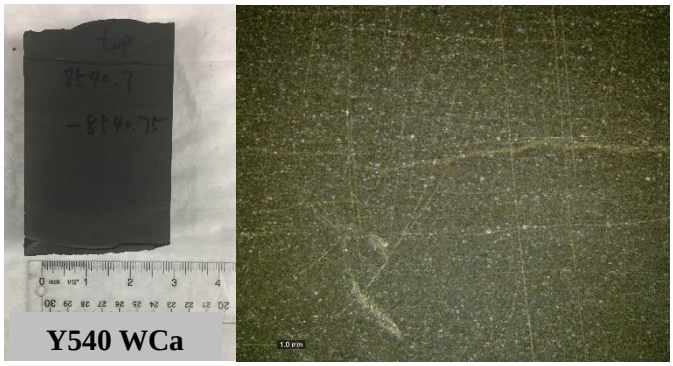

J

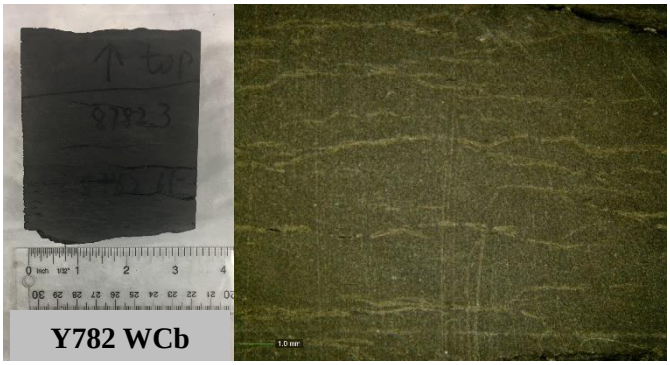

K

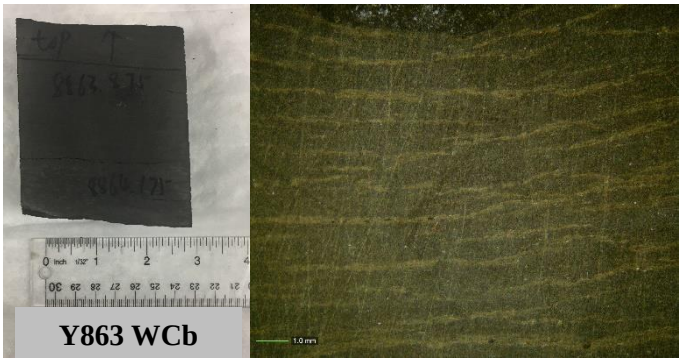

L

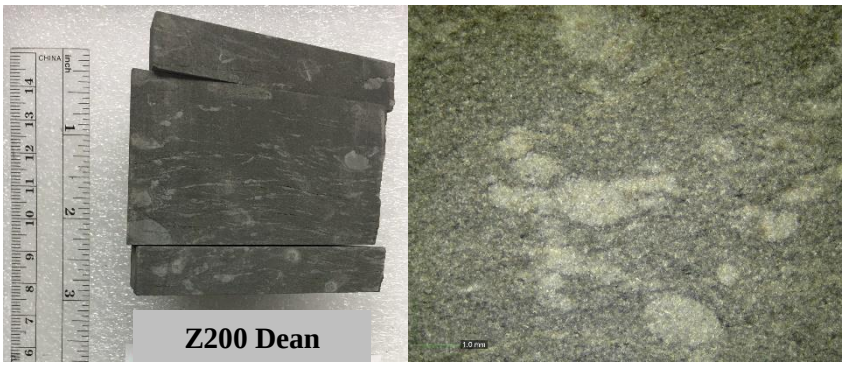

M

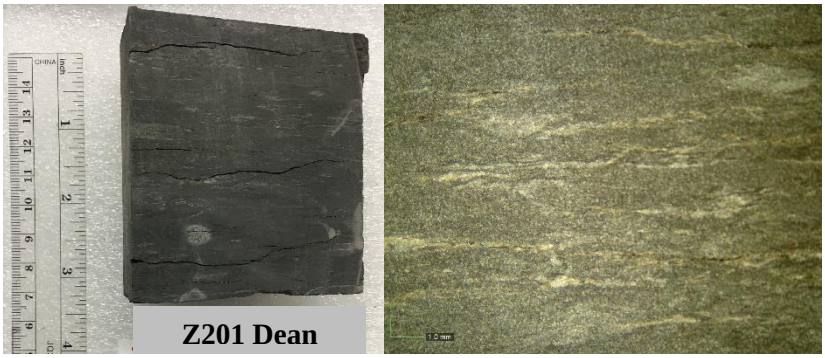

N

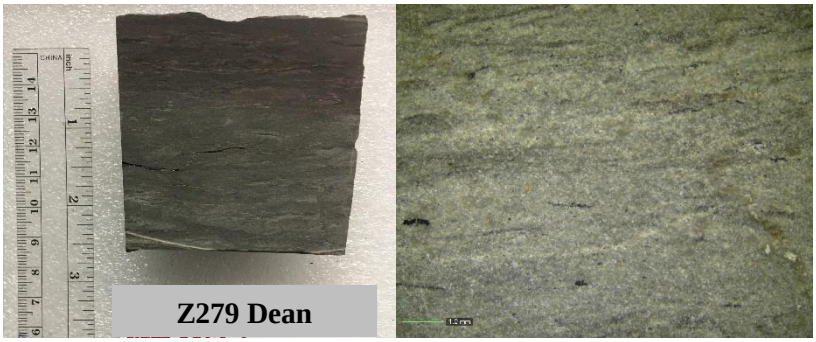

O

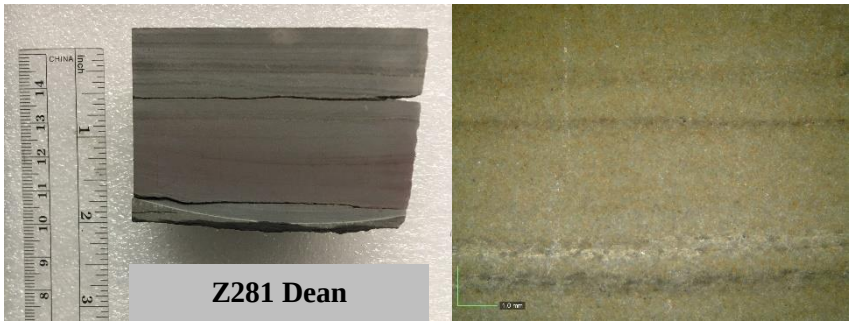

P

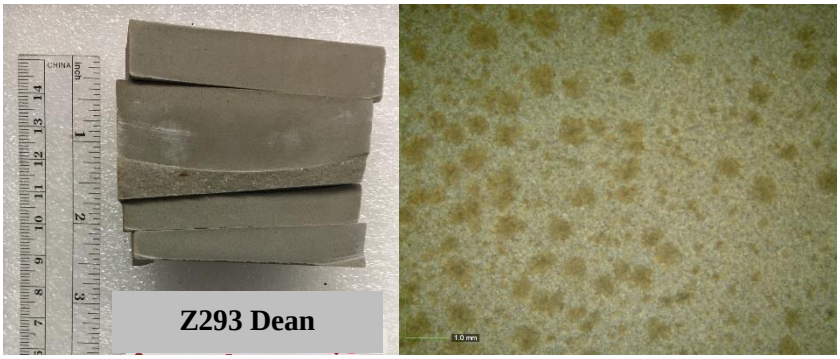

Q

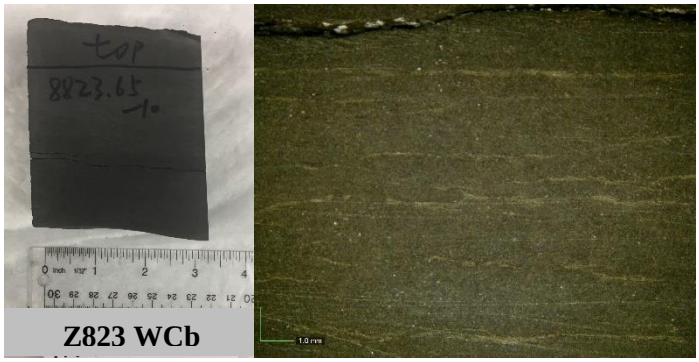

Figure 3-2 Photos upon sample arrival (left: zoomed out; right: zoomed in; scale bars displayed on each picture): (A) W537A SPRA; (B) W537B SPRA; (C) W766 SPRA; (D) W767 SPRA; (E) X340 WCa; (F) X461 WCa; (G) X682 WCa; (H) Y538 WCa; (I) Y540 WCa; (J) Y782 WCb; (K) Y863 WCb; (L) Z200 Dean; (M) Z201 Dean; (N) Z279 Dean; (O) Z281 Dean; (P) Z293 Dean; (L) Z823 WCb

Table 3-2 Tests performed on each sample

			Vacuum Saturation and Fluid		Imbibition		
Sample ID	XRD	Pyrolysis	Large Irregular Shape	$1cm^3$ Cubes	DI Water	DT2	MICP
W537A SPRA	✓	✓	✓	✓	✓	✓	✓
W537B SPRA	✓	✓	✓	✓	✓		
W766 SPRA	✓	✓	✓	✓	✓	✓	
W767 SPRA	✓	✓	✓	✓	✓	✓	
X340 WCa	✓	✓	✓	✓	✓		✓
X461 WCa	✓	✓	✓	✓	✓	✓	
X682 WCa	✓	✓	✓	✓	✓	✓	✓
Y538 WCa	✓	✓	✓	✓		✓	✓
Y540 WCa	✓	✓	✓	✓	✓		✓
Y782 WCb	✓	✓	✓	✓	✓	✓	✓
Y863 WCb	✓	✓	✓	✓	✓		✓
Z200 Dean	✓	✓	✓		✓		✓
Z201 Dean	✓	✓	✓		✓		
Z279 Dean	✓	✓	✓				
Z281 Dean	✓	✓	✓		✓	✓	✓
Z293 Dean	✓	✓	✓		✓		✓
Z823 WCb	✓	✓	✓	✓	✓	✓	✓

Note: DT2 = 2:1 volume mixture of n-decane and toulene

3-2 Geochemistry and Mineralogy

Geochemical analysis was performed by Weatherford Laboratories and the results were provided by Pioneer Natural Resources. The methods used for geochemical analysis is outlined in Appendix A – Methods and Procedures for Geochemical Analysis at Weatherford Laboratories. Data provided from the geochemical analysis includes total organic carbon (TOC) and several pyrolysis indices (e.g., S1, S2, S3, and T_{max}). S1 values are a measurement of the free hydrocarbons present in the sample before analysis and can be thought of as a residual hydrocarbon phase. S2 values are a measurement of the volume of hydrocarbons generated from thermal pyrolysis and can be thought of as the hydrocarbon generating potential of the sample. S3 are a measurement of the carbon dioxide generated from the thermal breakdown of kerogen. T_{max} is the highest temperature reached during the maximum evolution of S2 hydrocarbons and can be thought of as a measure of the source rock maturity. Geochemical analysis was performed at frequent and continuous intervals over the entire depth of the wells in this study. Geochemical analysis was not performed at the exact depths of the samples selected for this study, so well logs with TOC and pyrolysis values over the entire depth of each well were created and the TOC and pyrolysis values for each sample's discrete depth were interpolated from the well log curves. An example of a well log curve used to interpolate TOC and pyrolysis values is provided in Figure 3-3. Geochemical data was not provided from a significant range of depth which 5 samples were collected from in Well Z. These samples were sent to Geomark Laboratories where geochemical analysis was performed. Data provided from the geochemical analysis performed at Geomark Laboratories include TOC and several pyrolysis indices (e.g., S1, S2, S3, and T_{max}). The methods used by Geomark Laboratories for geochemical analysis is outlined in Appendix B – Laboratory Methods and Procedures for TOC and Pyrolysis Analysis at GeoMark Research.

X-Ray Diffraction (XRD) analysis was performed by Weatherford Laboratories and the results were provided by Pioneer Natural Resources. The methods for XRD analysis are outlined in Appendix C – Methods and Procedures for Geochemical Analysis at Weatherford Laboratories. XRD was performed at frequent and continuous intervals over the entire depth of the wells in this study. Bulk percentages of various minerals at each sample depth are provided from the analyses. XRD was not performed at the exact depths of the samples selected for this study so bulk mineralogical percentages at the exact depths of the samples were interpolated using the same method used to interpolate TOC and pyrolysis values for each sample's discrete depth. The interpolated bulk percentages were used in conjunction with the sCore Lithofacies for organic mudrock to determine the lithology of this study's samples (Gamero-Diaz et al., 2013).

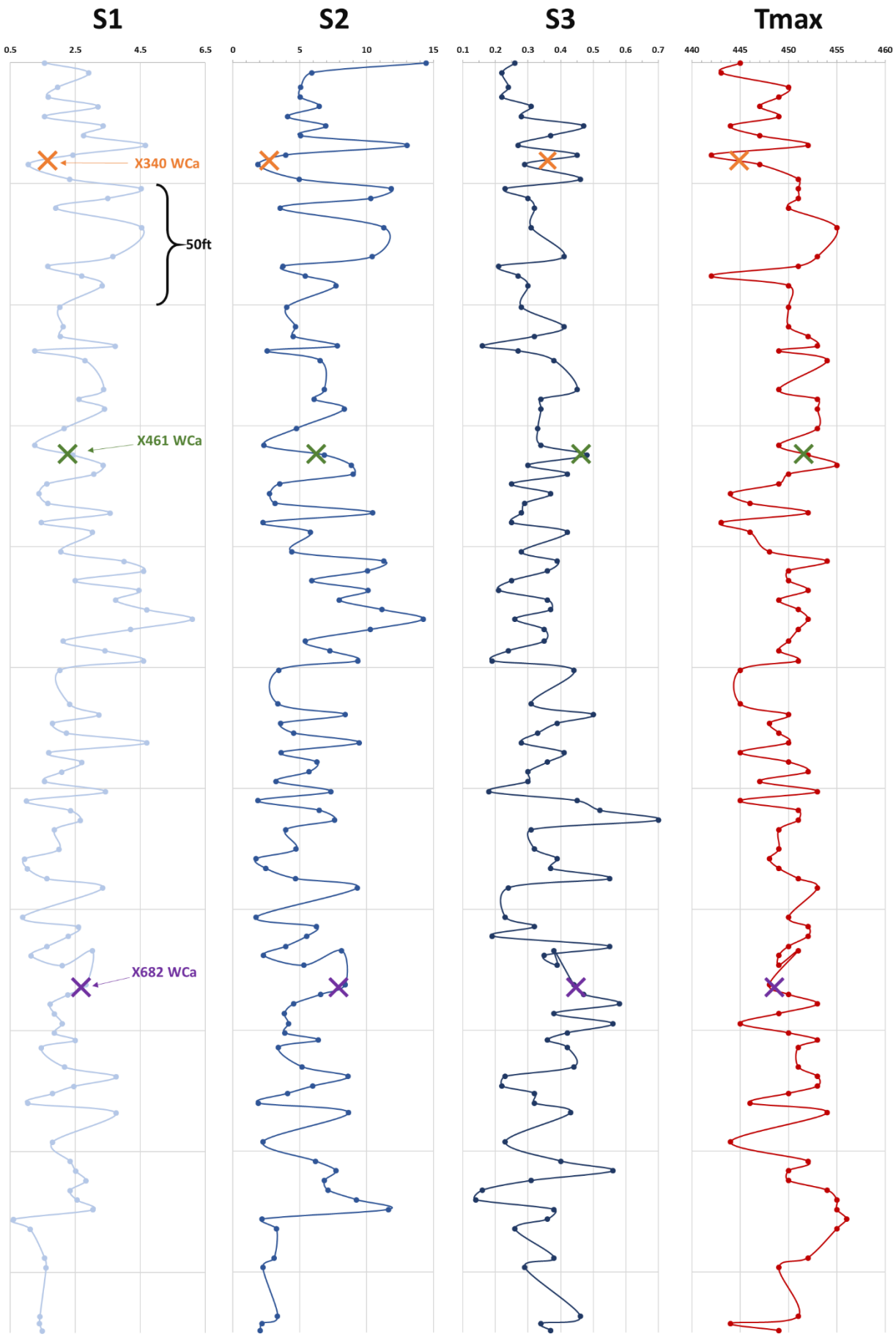

Figure 3-3 Example of well log curve interpolation method used to estimate pyrolysis indices

3-3 Vacuum Saturation and Liquid Displacement

Vacuum saturation and liquid displacement tests were performed to investigate the edge-only accessible porosity distribution of samples. An annotated image of the vacuum saturation apparatus is provided as Figure 3-5. The vacuum saturation apparatus consists of a sample chamber which is connected to a vacuum pump, compressed CO_2 gas cylinder, and reservoir of saturating fluid. The sample chamber is evacuated to 0.05 Torr and thus the air in edge-only accessible pores are evacuated. The sample chamber is also flushed with pressurized CO_2 during the evacuation process and immediately after the chamber is immersed with saturating fluid. Flushing the chamber with pressurized CO_2 during the evacuation process supports evacuation as it displaces air in edge connected pores with CO_2 which better dissolves in water. Flushing the chamber with pressurized CO_2 after the chamber is immersed with saturating assists with further driving the fluid into the edge-connected pores. After the evacuation and fluid immersion were complete, the saturated weight of the sample was recorded and then Archimedes' fluid displacement is utilized to determine bulk density, grain density, and porosity. Archimedes method employs an apparatus that consists of a basket that is suspended over an external support over an appropriately sized container of saturating fluid that sits on top of a loading balance. A simplified schematic of the apparatus used for Archimedes method is provided in Figure 3-6. The saturated sample was placed in the basket and fully submerged in the container of fluid after the loading balance was zeroed. The balance would measure an increase in mass equivalent to the mass of water displaced by the saturated sample's solids and voids and thereby provide all the components needed to determine the porosity, bulk density and grain density, using Equations 3.1, 3.2, 3.3, and 3.4 (Flint and Flint, 2002).

$$V_b = \frac{W_w}{\rho_w} \quad \text{Equation 3.1}$$

$$\emptyset = \frac{W_s - W_d}{V_b} \quad \text{Equation 3.2}$$

$$\rho_b = \frac{W_d}{V_b} \quad \text{Equation 3.3}$$

$$\rho_p = \frac{W_d}{V_b} - \emptyset \quad \text{Equation 3.4}$$

Where:

W_w = weight of water displaced from immersion of sample into fluid container (g)

ρ_w = density of fluid in fluid container (g/cm^3)

V_b = bulk volume of sample (cm^3)

W_s = saturated weight of sample (g)

W_d = dry weight of sample (g)

$\emptyset$ = porosity of sample (%)

P_b = bulk density of sample (g/cm^3)

P_p = particle density of sample (g/cm^3)

Vacuum Saturation and Liquid Displacement Procedure

Samples were dried in a 60°C oven for at least 48 hours before proceeding with vacuum saturation and liquid displacement tests. After being oven dried, the sample's oven dry weight was recorded, and the sample was immediately placed in a desiccator with less than 10% relative humidity and cooled to room temperature. The desired saturating fluid was prepared before

beginning the experiments. If saturating with water, DI water was boiled for 10 minutes, then cooled in a tightly sealed covered container until reaching room temperature. After the sample had cooled to room temperature, it was placed in the vacuum saturation sample chamber and the chamber was tightly sealed to ensure there were no leaks during the experiment. The valve connecting the chamber to the vacuum pump was opened, the vacuum pump was turned on and the chamber was evacuated for at least 8 hours. Pressure drawdown with respect to time in the chamber during the evacuation period was recorded. After the initial evacuation, the valve connecting the chamber to the vacuum pump was closed, the vacuum pump was temporarily turned off, the valve connecting the chamber to the CO_2 tank was opened and CO_2 was introduced into the chamber until the CO_2 gauge read 50psi. After the CO_2 gauge read 50psi, the valve connecting the chamber to the CO_2 tank was closed (which prevents leakage through the CO_2 hose) and CO_2 was released into the chamber for 30 minutes. After CO_2 had released into the chamber for 30 minutes, the valve connecting the chamber to the vacuum pump was re-opened, the vacuum pump is then turned on and the chamber is evacuated for another 12-18 hours. Pressure drawdown with respect to time in the chamber during the evacuation period was also recorded After the sample has been evacuated sufficiently (chamber evacuated to less than 0.2 Torr), the valve connecting the chamber to the vacuum pump was closed, and the vacuum pump was turned off. The fluid reservoir was then filled with enough de-aired DI water to immerse all samples in the chamber and then the valve connecting the chamber to the fluid reservoir was opened so that fluid could enter the chamber. After, all the samples in the chamber were immersed in fluid, the valve connecting the chamber to the fluid reservoir was closed, the valve connecting the CO_2 tank to the chamber was opened, and the chamber was introduced to CO_2 once more until the CO_2 gauge read 50psi. Afterwards, the valve connecting the CO_2 tank to

the chamber was closed and the samples were left to sit in the filled evacuated chamber for at least 8 hours. Afterwards, the chamber was opened, and the saturated weights of the samples were recorded. Archimedes' fluid displacement method was then immediately employed. The Archimedes' method apparatus was set up before the vacuum saturation experiment ended. Before placing the saturated sample into the pervious basket, the balance was zeroed with the empty pervious basket fully submerged in the fluid container. The basket was then raised, and the saturated sample was placed into the basket and fully submerged into the fluid container. The mass of the water displaced by the sample in the container was then recorded and the samples were placed back into the 60°C oven for 48 hours to get a second dry weight.

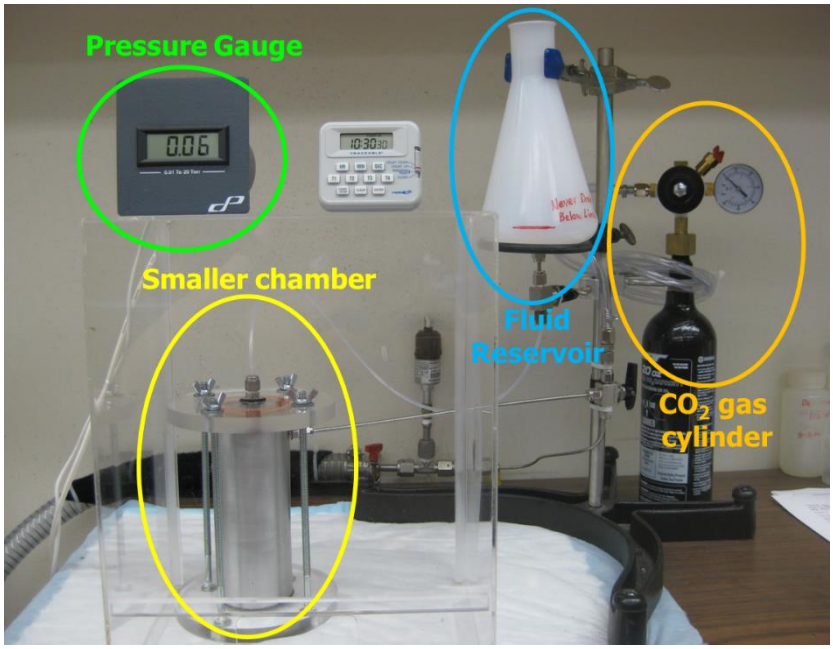

Figure 3-4 Vacuum saturation apparatus (Barber, 2014)

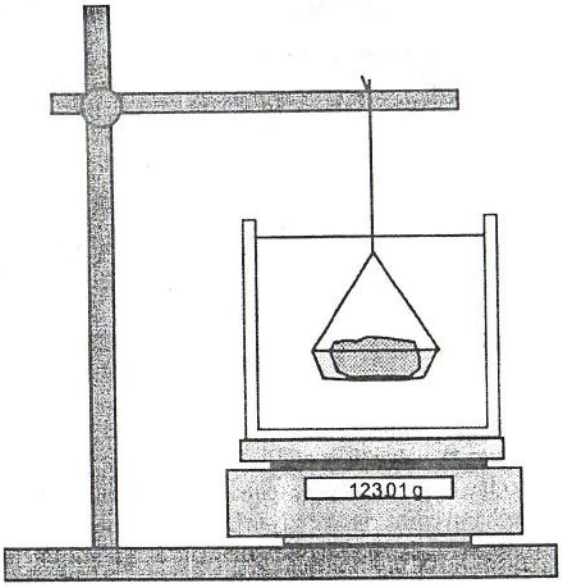

Figure 3-5 Simplified schematic of Archimedes method apparatus (Flint and Flint, 2002).

3-4 Spontaneous Fluid Imbibition

Spontaneous fluid imbibition is the process driven by capillary pressure that displaces a nonwetting fluid with a wetting fluid in a porous medium (Gao and Hu, 2012). In this study, the nonwetting fluid is air, and the wetting fluids are DI water and DT2 (n-decane: toluene=2:1 in volume). For porous media with well-connected pore space, the rate of imbibition can be quantified by sorptivity, the measure of the capacity of a medium to absorb or desorb a fluid by capillarity. Sorptivity is dependent on capillary pressure and permeability (Hu et al., 2001). As a fluid is imbibed through a sample, the cumulative uptake of water by imbibition with respect to time can be expressed by Equation 3.1 (Phillip, 1957; Hu et al., 2001).

$$I(t) = St^{0.5} + At \qquad \text{Equation 3.5}$$

Where:

I(t) = cumulative imbibition as a function of time (mm)

S = Sorptivity (mm/s)

A = empirically determined constant dependent on medium properties, initial water content, and boundary conditions (mm/s)

t = time (s)

According to Phillip (1957) the At term is negligible when the gravity potential gradients are small relative to matrix potential gradients (Hu et al., 2001). This is valid for all the imbibition tests of this study, considering the nm-sized pore sizes and ultra-small permeability of our shale samples. Pore connectivity affects the rate which the wetting front propagates into the sample. In samples with poor pore connectivity, the accessible porosity will decrease with distance from the sample edge and the wetting front will ultimately exhibit a slower imbibition rate as the fluid is imbibed through the sample. Samples with poor connectivity typically exhibit imbibition slopes of approximately 0.25 in log-log space (Hu et al., 2012). However, in samples where the accessible porosity is uniform with distance from the sample edge, samples will exhibit imbibition slopes of 0.5 in log-log space (Hu et al., 2012).

Spontaneous Fluid Imbibition Procedure

Samples were cut into approximately 1 cm^3 cubes for imbibition experiments. All the sides of the cubed sample except the top and bottom were then covered with quick-cure epoxy. Epoxying the cubed sample's sides prevents evaporation/absorption from the side surfaces and helps imbibition to occur in only one direction. Before beginning imbibition experiments, several things must be accomplished. First, samples were dried in a 60°C oven for at least 48 hours and then immediately placed in a desiccator with less than 10% relative humidity and cooled to the room temperature. The sample's oven dry weight, sample and holder weight, holder weight only, and dish and fluid weight were then recorded. Several beakers of DI water were placed in the

experiment chamber to main a constant and high relative humidity. The sample was then tightly secured onto the holder and then suspended over a hook in the chamber that connects the holder to bottom-weighing electronic balance. A simplified schematic of the imbibition apparatus is shown in Figure 3-4. The dish containing fluid was then placed into the lowered chamber, the chamber was closed, and then the chamber was raised until sample bottom was submerged to a depth of approximately 1mm in the fluid reservoir. Immediately after the sample was submerged to a depth of 1mm the rate of imbibition rate was monitored by recording the change of weight in the sample over time. Sample weight was recorded every second for the first two minutes, then recorded every 30 seconds from the elapsed time interval of 2 minutes to 1 hours, then recorded every 2 minutes for the elapsed time interval of 1 hour to 6 hours, and then recorded every 5 minutes for the duration of the experiment. DT2 imbibition experiments were run for 8 hours and DI water imbibition for 24 hours. Spot checks were periodically conducted with a timer to confirm the accuracy of the time and weight recorded by the computer. After the imbibition experiment was completed, the sample chamber was lowered so that the sample was no longer in contact with the fluid reservoir. The sample and holder were then removed from the hook attaching them to the bottom-weighing electronic balance and any excess fluid was wiped off with an already weighed Kimwipe that has been moistened with the testing fluid. The Kimwipe used to wipe of the excess fluid from the sample bottom was then promptly weighed again to record the amount of excess fluid. The sample and holder, sample only, and holder only weights were then obtained to check against effects of buoyancy and any fluid potentially condensed on the sample holder. Lastly, the dish containing fluid was re-weighed to determine the effects of evaporation.

The rates of imbibition were determined by plotting log cumulative imbibition with respect to log time using the acquired data. Buoyancy and evaporation corrections were made to the acquired data using the weights obtained before and after the imbibition experiments. Slope lines were then fitted at various periods during the imbibition experiment. Typically, four distinct slopes could be observed over the duration of the imbibition experiment. The first slope is typically observed at the very beginning of the experiment and lasts several seconds. This slope generally has a value between 2-4 and is related to the initial adherence of the fluid to samples bottom which creates a fluid meniscus. The second slope is observed directly after the first slope and usually lasts several minutes. This slope generally has a value that are two-thirds of the initial slope and is related to the testing fluid migrating through the sample's microfractures, lamination, and edge. The third slope, also known as the "connectivity" slope, lasts several hours and is associated with pore connectivity in the sample's interior. Expected values for the third slope range from 0.25 to 0.5. The fourth slope is generally observed towards the end of the experiment and is associated with the fluid front reaching the top. The expected value for the fourth slope is approximately 0.1.

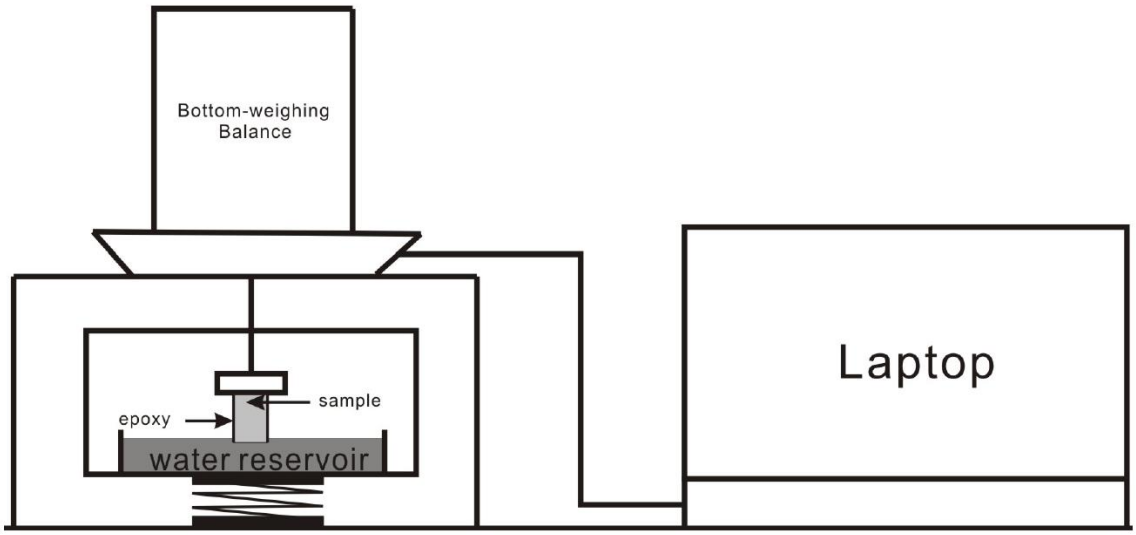

Figure 3-6 Simplified schematic of imbibition apparatus (Gao and Hu, 2012)

3-4 Mercury Intrusion Capillary Pressure

MICP was performed using a Micrometrics Autopore IV 9520 instrument (Figure 3-7). The MICP method is particularly useful because it allows for the characterization of several parameters over nano-μm scale which is essential in shales which have notable pore size distribution in the nanometer range. Parameters obtained from MICP analysis include bulk density, particle density, pore surface area, porosity, pore-throat size distributions. In addition, permeability, and tortuosity can be indirectly obtained from MICP. The MICP method involves placing a sample into a penetrometer and then forcing mercury, a non-wetting fluid, into the pores of a sample at pressures up to 60,000 psia (414 MPa). These high pressures are large enough to exceed the capillary pressure and thereby enable mercury to invade samples' pore throats. Incremental changes in pressure in the penetrometer are then measured and used to calculate pore size distribution. The Washburn equation (Equation 3-1) demonstrates that the intruded pore throat radius is inversely proportional to the applied external pressure (Washburn, 1921; Gao and Hu, 2013).

$$\Delta P = -\frac{2\gamma \cos\theta}{R} \qquad \text{Equation 3.6}$$

Where:

ΔP = External pressure applied (psia)

γ = Surface tension of mercury (dynes/cm)

θ = Contact angle between mercury and pore wall (degrees)

R = Pore throat radius (μm)

Equation 3.1 assumes that the values for surface tension and contact angle remain constant. However, recent study of Wang et al. (2016) suggested that the contact angle between mercury and the pore wall as well as the surface tension of mercury vary significantly as pore size decreases and ignoring this variability could produce relative errors as high as 44% (Wang et al., 2016). Therefore, a modified Washburn equation that considers the variability of mercury contact angle and surface tension with respect to pore throat size is needed. The modified Washburn equation is displayed below (Equation 3.2), where surface tension and contact angle are now functions of the pore throat radius (R). The function of R is provided by Equation 3.3.

$$\Delta P = -\frac{2\gamma_{Hg}(R)\cos\theta_{Hg}(R)}{R} \qquad \text{Equation 3.7}$$

$$f(R) = p_c R + 2\gamma_{Hg}(R)\cos\theta_{Hg}(R) \qquad \text{Equation 3.8}$$

Where:

p_c = Capillary pressure of the intruded pore

The modified Washburn equations simply assumes that all pores are cylindrical. However, doing so allows mercury pressure to be converted to an equivalent pore throat diameter and thereby provides a close approximation of pore throats in shales (Hu et all., 2015). The range of pore-throat diameters that can be examined is 2.8 nm to about 1000 μm.

Permeability and tortuosity can be indirectly determined from MICP tests by utilizing various methods. Katz and Thompson's (1986) method (Equation 3.4) is used to estimate permeability.

$$k = \frac{1}{89}(L_{max})^2 \frac{L_{max}}{L_c} \emptyset S(L_{max})$$ Equation 3.9

Where:

k = Permeability (μm^2)

L_{max} = Pore throat diameter when hydraulic conductance is at a maximum, when mercury percolates through the whole sample after overcoming capillary pressure of a specific pore diameter (μm)

L_c = Pore throat diameter. Determined by inflection point on MICP intrusion curve (μm)

∅ = Sample porosity (fractional)

$S(L_{max})$ = Mercury saturation at percolation (ratio of cumulative intrusion at L_{max} to total pore volume)

MICP Procedure

Samples were dried in a 60°C oven for at least 48 hours before proceeding with MICP tests. After being oven dried, the sample was immediately placed in a desiccator with less than 10% relative humidity and cooled to room temperature. Once the sample was cooled, it was placed into an apparatus referred to as penetrometer and then the sample and penetrometer was inserted into the Micrometrics Autopore IV 9520 machine where it was evacuated to 6.7 Pa. After being evacuated, the sample was subjected to the first of two different analyses. The first analysis was a low-pressure intrusion test from 5 psi to 30 psi which detects larger pores around 50 μm. Pressure was introduced into the penetrometer in incremental steps from 5 psi to 30 psi. Between each step, 10 seconds of equilibrium time was given so that mercury in the sample stabilized before the next pressure was applied. After this analysis was complete, the sample and

penetrometer weight were recorded as not all the mercury would extrude after the test completion. The second analysis was a high-pressure intrusion test from 30 psi to 60,000 psi. Equilibrium time between each pressure step during this analysis was 45 seconds. The extrusion curve of mercury as the pressure drops was also recorded.

Figure 3-7 Micrometrics autopore IV 9520 instrument

3-6 Production Data

Monthly production data for the four wells in this study were acquired through a complimentary subscription of Drilling Info provided to Dr. Qinhong Hu's research group at the University of Texas at Arlington.

Chapter 4 – Results

4-1 Mineralogy

The mineral composition of the samples is dominated by quartz, carbonate minerals, clay minerals, and plagioclase feldspar. Minor quantities of potassium feldspar, sulfide minerals, and apatite minerals are found in the samples. Whole rock mineralogy and clay mineralogy are presented in Table 4-1 and Figure 4-1. In Figure 4-2, the weight percentages of clays (illite, smectite, mica, and chlorite), QFM (quartz, plagioclase, and potassium feldspar), and carbonates (calcite, dolomite, and siderite) were plotted on sCore Lithofacies' ternary diagram for the classification of organic mudrocks (Gamero-Diaz et al., 2013). Six different lithotypes are observed in the sample set. Samples from Wolfcamp B plotted within the clay-rich siliceous mudstone or mixed siliceous mudstone lithotypes. The lithology of samples from the Wolfcamp A Formation is found to be the most heterogenous in the sample set. Lithology in the Wolfcamp A samples vary from lithotypes with relatively high weight percentages of carbonates such as carbonate/siliceous mudstone and silica-rich carbonate mudstone or lithotypes with greater weight percentages of quartz-feldspar minerals and clay minerals such as mixed mudstone and clay-rich siliceous mudstone. Samples from the Dean and Spraberry Formation plotted within four different lithotypes, all are lithotypes which quartz-feldspar is the most prevalent end-member, except for one sample that plotted within the carbonate/siliceous mudstone lithotype.

Table 4-1 Whole rock mineralogy and clay mineralogy of samples

	Whole Rock Mineralogy (wt. %)										Clays (wt. %)			
Sample ID	**Quartz**	**K-Feldspar**	**Plagioclase**	**Calcite**	**Dolomite**	**Siderite**	**Apatites**	**Pyrite**	**Marcasite**	**Total Clay**	**Illite/Smectite**	**Illite/Mica**	**Chlorite**	**Lithofacies**
W537A SPRA	32.5	5.8	14.9	10.4	2.9	0.9	1.9	1	-	29.7	4.4	24.3	1.1	Mixed siliceous mudstone
W537B SPRA	33.6	5.4	14.6	9	2.6	0.8	1.6	1	-	31.4	5.2	25.0	1.2	Mixed siliceous mudstone
W766 SPRA	46.1	7.7	14.2	3.8	3	-	0.6	1.4	-	23.2	3.6	17.5	2.0	Clay-rich siliceous mudstone
W767 SPRA	43.9	6.3	14.5	3.5	3	-	1.4	1.9	-	25.5	4.4	19.2	2.0	Clay-rich siliceous mudstone
X340 WCa	22.9	0.4	6.4	52.9	4.6	-	1.6	2.3	-	9	1.6	7.4	-	Silica-rich carbonate mudstone
X461 WCa	31.7	1	7.1	21.9	7.1	-	-	2.5	-	28.7	5.5	23.2	-	Mixed mudstone
X682 WCa	33.3	0.9	15.6	1.1	5.6	-	11.9	2.6	-	29.1	7.6	21.5	-	Clay-rich siliceous mudstone
Y538 WCa	38.9	1.5	6.9	28	6.8	-	-	2.1	0.7	15	2.5	12.5	-	Carbonate/siliceous mudstone
Y540 WCa	35.24	1.55	5.54	35.5	5.95	-	-	2.02	0.78	13.22	2.6	10.6	-	Carbonate/siliceous mudstone
Y782 WCb	44.47	1.43	8.69	12.79	8.34	-	0.25	2.69	0.6	21.4	3.8	17.6	-	Mixed siliceous mudstone
Y863 WCb	54.12	1.06	6.86	11.23	4.92	-	-	2.27	-	19.53	2.2	10.0	-	Mixed siliceous mudstone
Z200 Dean	46.1	1.6	9.6	-	28.8	-	-	1.6	-	12.2	3.0	9.2	-	Mixed siliceous mudstone
Z201 Dean	47.5	1.7	9.7	-	26.9	-	-	1.7	-	12.5	3.0	9.5	-	Mixed siliceous mudstone
Z279 Dean	37	1.5	8.6	-	31.1	1	-	2	-	18.7	4.5	13.2	1.0	Carbonate/siliceous mudstone
Z281 Dean	45.2	1.8	10.9	-	16.7	1	-	2.5	-	21.9	5.3	15.6	1.0	Mixed siliceous mudstone
Z293 Dean	64	2	14.8	-	6.7	0.1	-	1.2	-	11.3	2.3	8.9	0.1	Silica dominated lithotype
Z823 WCb	58.2	-	3.9	2.9	4.3	0.6	-	5.8	-	24.3	5.6	18.7	-	Clay-rich siliceous mudstone

W537A SPRA

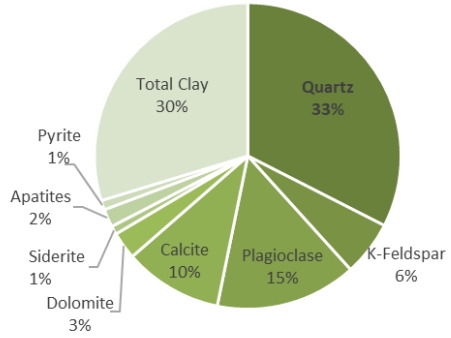

W537B SPRA

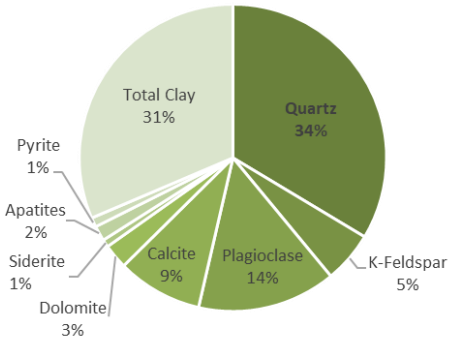

W766 SPRA

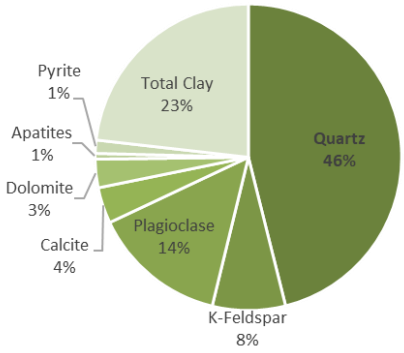

W767 SPRA

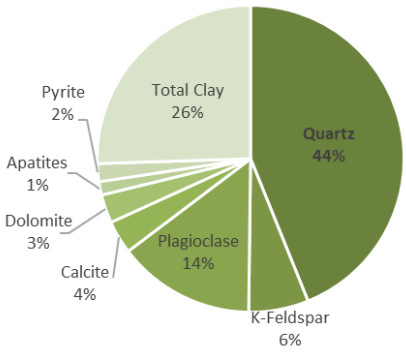

X340 WCa

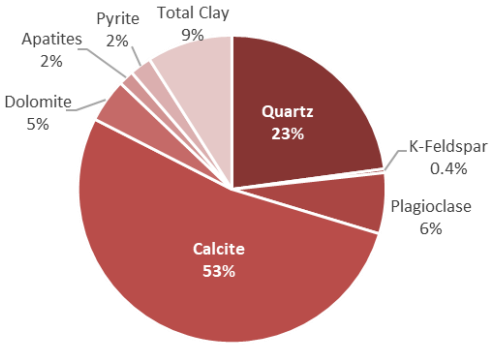

X461 WCa

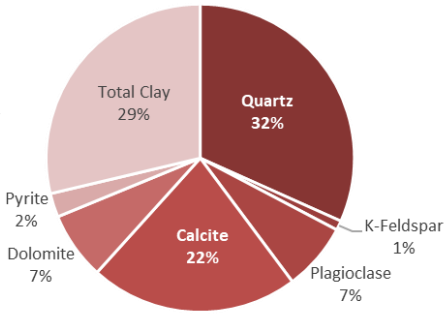

X682 WCa

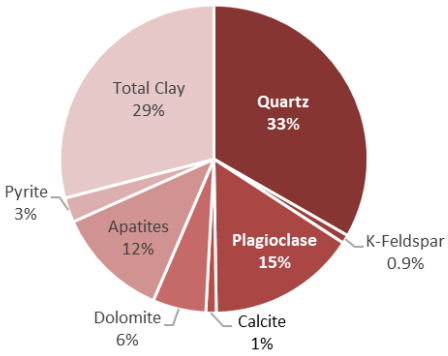

Y538 WCa

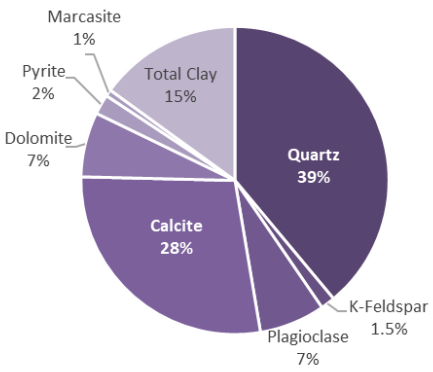

Y540 WCa

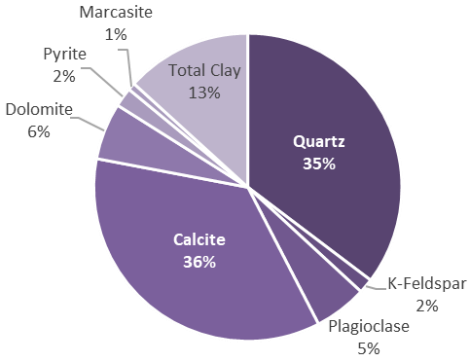

Y782 WCb

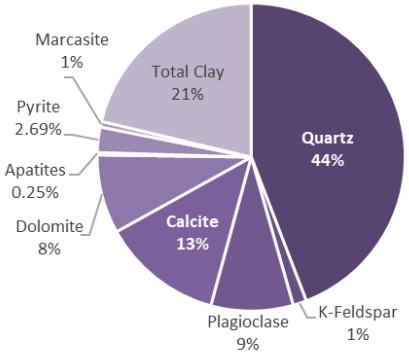

Y863 WCb

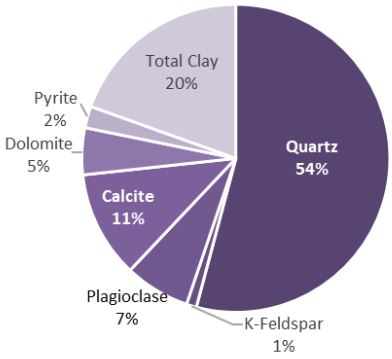

Z200 Dean

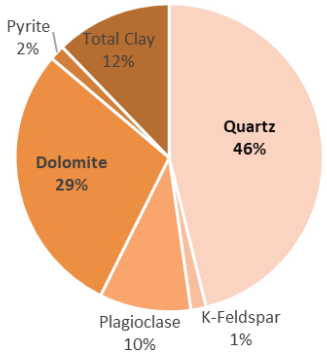

Z201 Dean

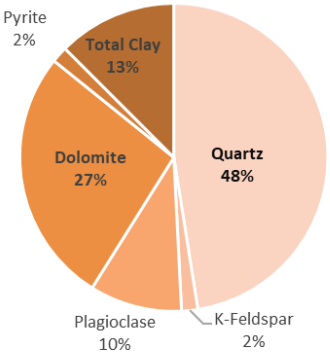

Z279 Dean

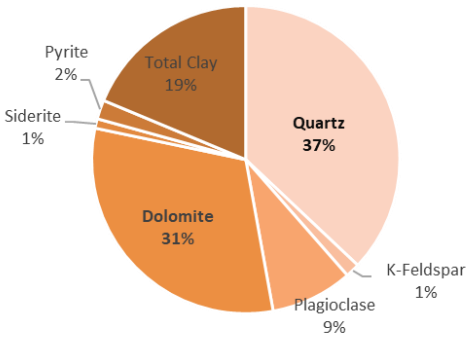

Z281 Dean

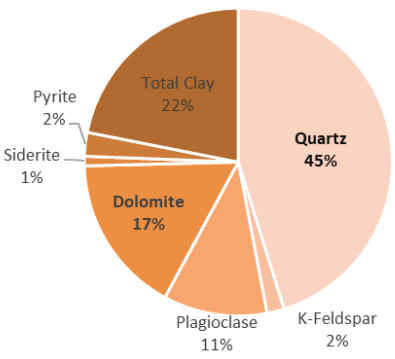

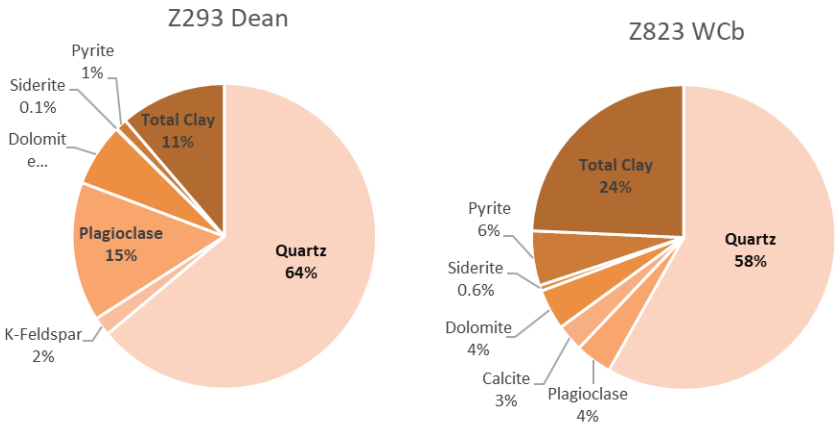

Figure 4-1 Whole Rock mineralogy of samples

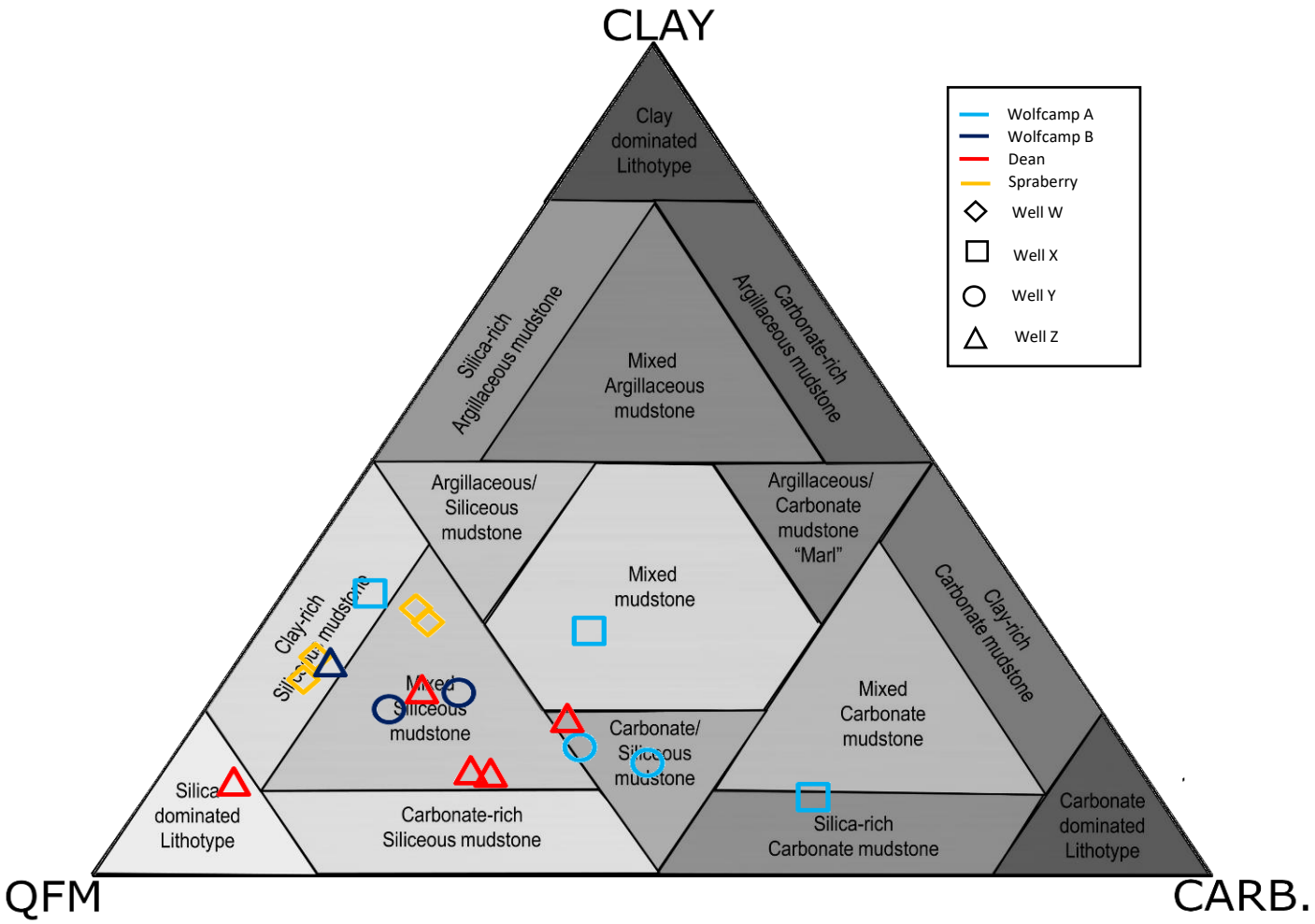

Figure 4-2 Samples from all wells plotted on diagram for sCore lithofacies classification scheme for organic mudstones (Gamero-Diaz et al., 2013).

4-2 Geochemistry

Geochemical data for the sample set are displayed in Table 4-2. TOC weight percentages in all the samples range from 0.07% to 3.36%. Ranging from 0.07% to 0.61%, TOC weight percentages in samples collected from the Dean Formation where significantly lower than the rest of the sample set. S1 values, the mass of residual hydrocarbons currently present per unit mass of rock, range from 0.02 mg/g to 3.70 mg/g. S2 values, the mass of hydrocarbons that formed during thermal pyrolysis per unit mass of rock, range from 0.07 mg/g to 8.94 mg/g. T_{max} values range from 432°C to 452°C. The lowest average values of S1 S2, and T_{max} are observed in the samples collected from the Dean Formation. The highest average TOC, S1, and S2 values are observed in samples collected from Wolfcamp B. The kerogen type and maturity of all samples are determined by calculating the hydrogen index of samples form pyrolysis results and then plotting T_{max} values of the samples vs. the hydrogen index of the samples; kerogen type and maturity results are presented in Figure 4-3. Most samples, except for samples from the Dean Formation, are type II kerogens in the oil window. Dean samples are immature and mature Type III kerogens.

Table 4-2 Geochemical analyses of samples.

Sample ID	TOC (%)	S1 (mg/g)	S2 (mg/g)	S3 (mg/g)	T_{max} (°C)	Vitrinite Equivalency (from T_{max})	Hydrogen Index	Oxygen Index	S2/S3 Conc	S1/TOC	Production Index
W537A SPRA	2.48	1.73	8.45	0.29	446	0.87	341	11.6	29.5	70	0.17
W537B SPRA	2.36	1.71	8.82	0.28	445	0.86	373	11.9	31.5	73	0.16
W766 SPRA	1.36	1.59	3.24	0.16	444	0.83	239	11.7	20.5	117	0.33
W767 SPRA	1.29	1.57	3.21	0.09	444	0.83	249	7.2	34.3	122	0.33
X340 WCa	1.25	1.64	2.73	0.36	445	0.85	218	28.7	7.6	131	0.38
X461 WCa	2.57	2.26	6.23	0.46	452	0.97	243	18.0	13.5	88	0.27
X682 WCa	3.07	2.68	7.91	0.45	449	0.91	257	14.6	17.7	87	0.25
Y538 WCa	2.53	2.77	6.24	0.24	449	0.92	247	9.6	25.7	110	0.31
Y540 WCa	2.66	2.75	6.37	0.26	450	0.93	240	9.9	24.2	104	0.30
Y782 WCb	3.29	3.24	8.37	0.39	449	0.92	254	11.8	21.5	99	0.28
Y863 WCb	3.36	3.25	7.46	0.20	449	0.92	222	5.8	38.0	97	0.30
Z200 Dean	0.44	0.14	0.43	0.39	443	0.81	97	87.8	1.1	32	0.25
Z201 Dean	0.61	0.21	0.72	0.33	442	0.80	117	53.7	2.2	34	0.23
Z279 Dean	0.30	0.08	0.21	0.31	437	0.71	70	104.0	0.7	27	0.28
Z281 Dean	0.22	0.08	0.15	0.36	441	0.78	68	162.9	0.4	36	0.35
Z293 Dean	0.07	0.02	0.07	0.35	432	0.62	97	486.8	0.2	28	0.22
Z823 WCb	3.26	3.70	8.94	0.14	444	0.83	274	4.3	63.8	114	0.29

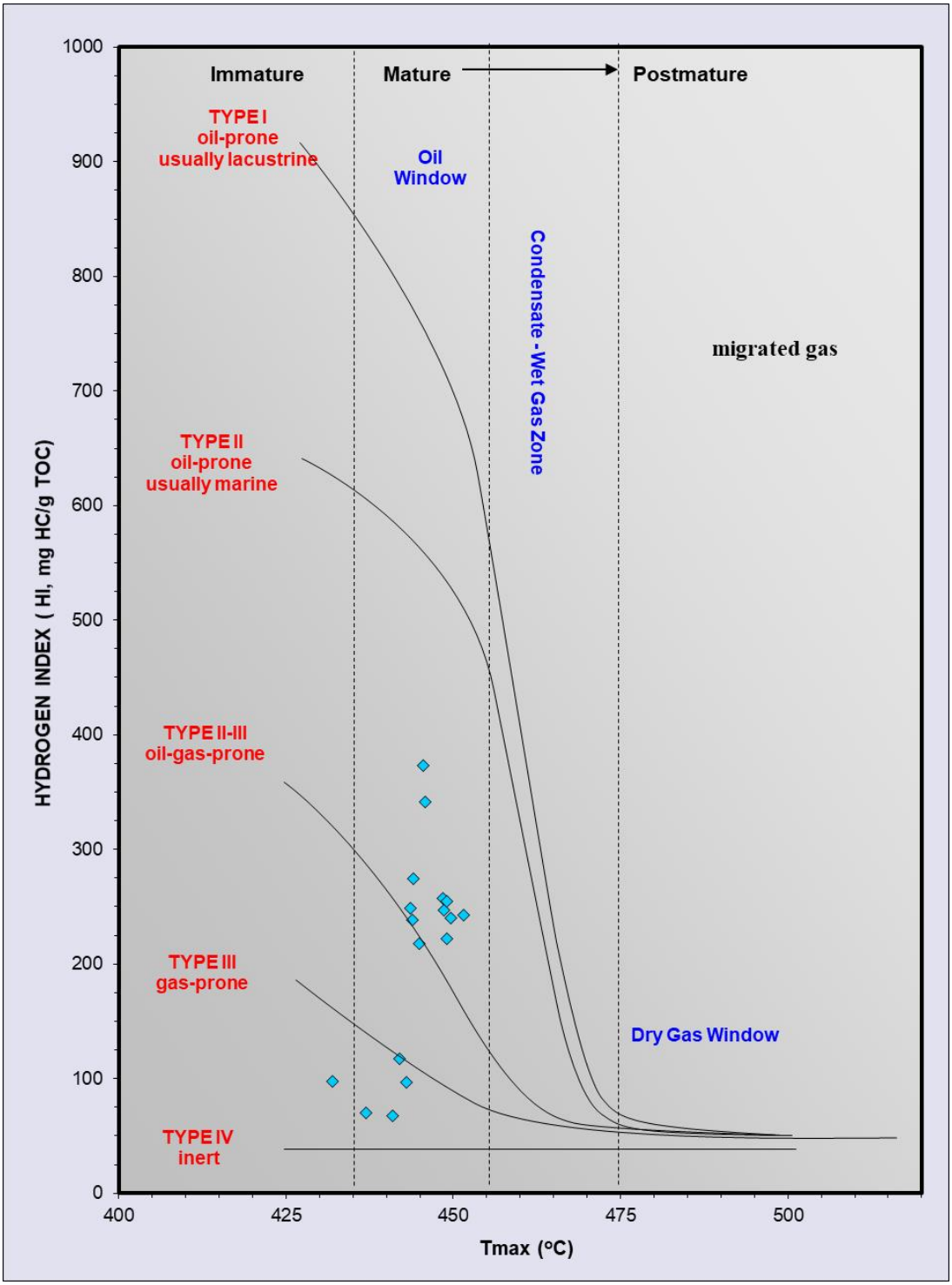

Figure 4-3 Kerogen type and maturity of samples

4-3 Vacuum Saturation and Liquid Displacement

Porosities, bulk densities, and grain densities obtained from vacuum saturation and liquid displacement tests of large irregular shaped samples and 1-cm cube samples are presented in Table 4-5. Samples collected from the Dean and Wolfcamp B Formation exhibit the highest porosities from the sample set. Dean and Wolfcamp B samples have porosities that range from 3.55% to 9.45% in large-sized and irregularly-shaped samples. Samples collected from the Spraberry and Wolfcamp A Formation exhibited the lowest porosities from the sample set. Spraberry and Wolfcamp A samples have porosities that range from 0.183% to 3.76% in large and irregularly-shaped samples. As the sample size is reduced, an increase in porosity is observed in most of the samples. This is most likely a result of pores that were once isolated from edge-accessible pore system being incorporated into the effective porosity of the sample after the sample is reduced in size.

Table 4-3 Porosity, bulk density, and grain density of samples from vacuum saturation tests with DI water

	Irregular			**Cubes**		
	Bulk density (g/cm^3)	Grain density (g/cm^3)	Porosity (%)	Bulk density (g/cm^3)	Grain density (g/cm^3)	Porosity (%)
W537A SPRA	2.635	2.646	0.430	2.587 ± 0.025	2.612 ± 0.018	0.963 ± 0.371
W537B SPRA	2.596	2.613	0.641	2.495 ± 0.077	2.535 ± 0.096	0.871 ± 0.081
W766 SPRA	2.522	2.551	1.135	2.508 ± 0.028	2.538 ± 0.025	1.197 ± 0.161
W767 SPRA	2.545	2.558	0.533	2.537 ± 0.032	2.563 ± 0.037	1.019 ± 0.191
X340 WCa	2.609	2.617	0.308	2.647 ± 0.033	2.665 ± 0.034	0.707 ± 0.193
X461 WCa	2.612	2.624	0.468	2.525 ± 0.062	2.550 ± 0.063	0.971 ± 0.112
X682 WCa	2.456	2.552	3.764	2.415 ± 0.097	2.503 ± 0.037	3.569 ± 2.856
Y538 WCa	2.678	2.683	0.183	2.698 ± 0.029	2.717 ± 0.029	0.673 ± 0.100
Y540 WCa	2.451	2.461	0.394	2.404 ± 0.007	2.449 ± 0.008	1.863 ± 0.269
Y782 WCb	2.308	2.513	8.153	2.322 ± 0.025	2.539 ± 0.035	8.536 ± 2.154
Y863 WCb	2.313	2.488	7.007	2.342 ± 0.168	2.531 ± 0.193	7.468 ± 0.414
Z200 Dean	2.503	2.676	6.486	-	-	-
Z201 Dean	2.409	2.660	9.448	-	-	-
Z279 Dean	2.478	2.682	7.634	-	-	-
Z281 Dean	2.578	2.682	3.890	-	-	-
Z293 Dean	2.478	2.697	8.098	-	-	-
Z823 WCb	2.290	2.374	3.554	2.401 ± 0.290	2.564 ± 0.316	6.326 ± 0.625

4-4 Spontaneous Fluid Imbibition

Spontaneous fluid imbibition tests using both DI water and DT2 were conducted on 7 samples. Spontaneous fluid imbibition tests with at least one fluid were conducted on every sample except for Z279 Dean. Results from the tests are presented in Table 4-3. Of the 7 samples which both DI water and DT2 imbibition tests were conducted, every sample, except for Y782 WCb, has a larger stage 3 slope with DT2 as the wetting fluid. Most samples exhibit a low pore connectivity when DI water is used as the wetting fluid. Of the 15 samples which imbibition tests with DI water were conducted, only 3 samples exhibit a high pore connectivity. Of the 8 samples which imbibition tests with DT2 water were conducted, 4 samples exhibit a high pore connectivity. Several samples exhibit imbibition slopes of approximately 0.5. Sorptivity values from cumulative imbibition during Stage 3 were calculated and then used to estimate permeability in the samples. The calculated sorptivity values and estimated permeability values are presented in Table 4-4.

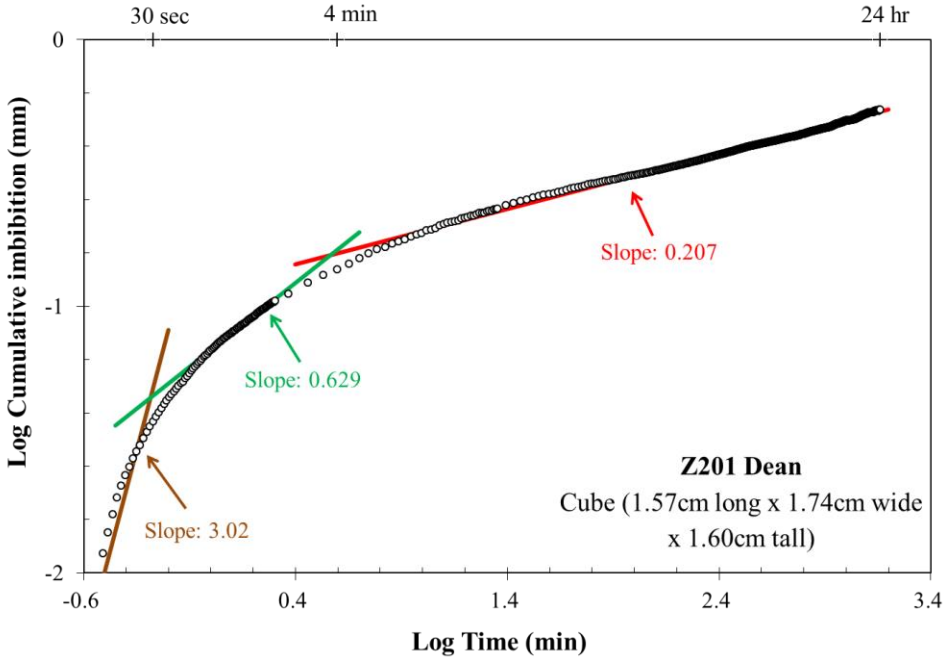

Figure 4-4 Example of DI water imbibition (Z201 Dean) with three stages of imbibition present.

Table 4-4 Stage III connectivity slopes from imbibition tests

Sample ID	Fluid	Connectivity Slope
W537A SPRA	DI water	0.233
	DT2	0.237
W537B SPRA	DI water	0.241
	DT2	-
W766 SPRA	DI water	0.247
	DT2	0.289
W767 SPRA	DI water	0.287
	DT2	0.554
X340 WCa	DI water	0.293
	DT2	-
X461 WCa	DI water	0.140
	DT2	0.255
X682 WCa	DI water	0.313
	DT2	0.412
Y538 WCa	DI water	-
	DT2	0.319
Y540 WCa	DI water	0.401
	DT2	-
Y782 WCb	DI water	0.532
	DT2	0.338
Y863 WCb	DI water	0.260
	DT2	-
Z200 DEAN	DI water	0.154
	DT2	-
Z201 DEAN	DI water	0.207
	DT2	-
Z279 DEAN	DI water	-
	DT2	-
Z281 DEAN	DI water	0.331
	DT2	0.430
Z293 DEAN	DI water	0.729
	DT2	-
Z823 WCb	DI water	0.351
	DT2	0.729

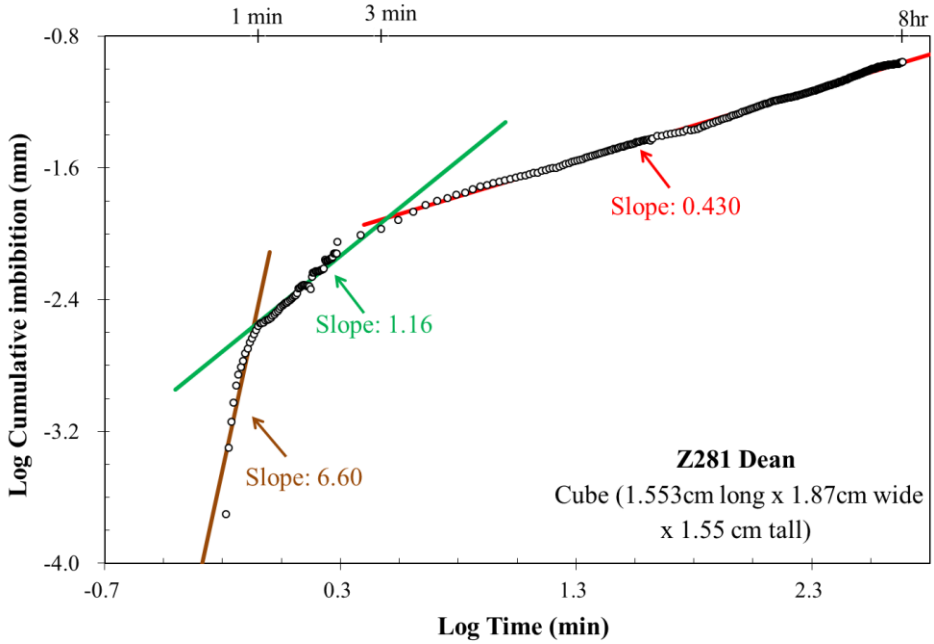

Figure 4-5 Example of DT2 imbibition (Z281 Dean) with three stages of imbibition present.

Table 4-5 Estimated permeabilities from sorptivity

Sample ID	Imbibition Fluid	Sorptivity ($m/sec^{0.5}$)	Permeability (nD)
W767 SPRA	DT2	9.02E-07	885
X682 WCa	DT2	1.23E-06	71.8
Y540 Wca	DI	4.99E-07	0.445
Y782 WCb	DI	2.36E-06	2.06
Z281 Dean	DT2	6.27E-07	2.94
Z293 Dean	DI	4.90E-07	0.012
Z823 WCb	DT2	3.50E-06	8.43

4-5 Mercury Intrusion Capillary Pressure

MICP analyses directly and indirectly provide a suite of invaluable information about the pore structure of the sample set. MICP analysis was conducted once on 11 of the 17 total samples. A summary of several pore characteristics obtained from MICP is presented in Table 4-6. Porosities in the samples range from 0.325% to 12.6%. Samples collected from the Dean and Wolfcamp B Formations exhibit the highest porosities whereas samples from the Spraberry and Wolfcamp A Formations show the lowest porosities. Similarly, samples collected from the Dean and Wolfcamp B Formations generally exhibit the highest total pore volumes with total pore volume ranging from 11.6 mm^3/g to 57.3 mm^3/g. Apart from one Wolfcamp A sample which has a fairly large total pore volume, samples collected from the Spraberry and Wolfcamp A Formations exhibit total pore volumes ranging from 1.2 mm^3/g to 10.6 mm^3/g.

Pore throat distribution in the samples were determined by identifying inflection points from the log differential vs. intrusion pressure curves from the MICP data and using the corresponding information in conjunction with the modified Washburn equation. Inflection points on the log differential vs. intrusion pressure curves are discrete points which rapid

increases followed with decreases in intrusion volume occur. An inflection point represents the moment which the capillary pressure required to invade a specific pore size has been overcome.

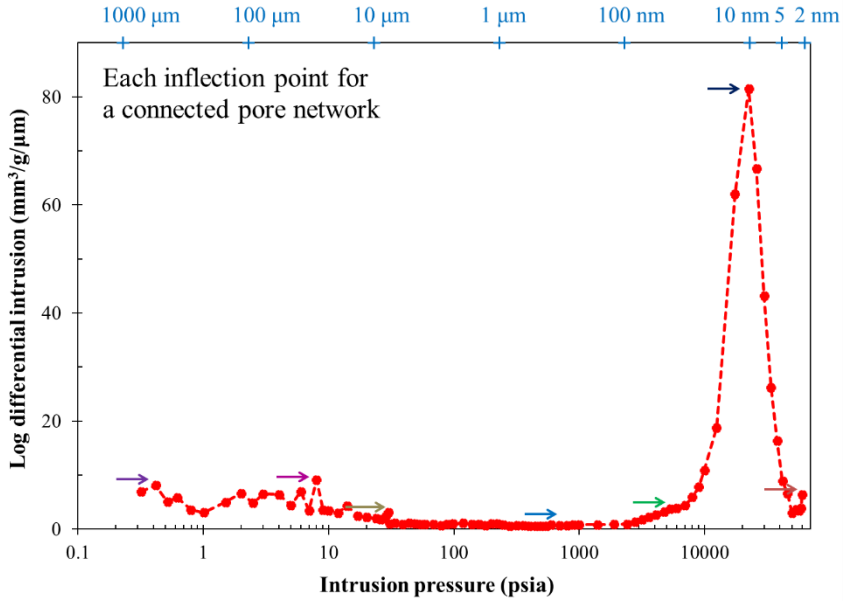

Figure 4-6 Example showing inflection points in MICP intrusion for Z823 WCb; colored arrows indicate inflection points.

Figure 4-6 is an example of an inflection point from the processed MICP data. The pore size distribution of the samples is presented in Figure 4-7 and Table 4-7. Different pore throat diameters are qualitatively associated with different pore systems in shales (Hu et al., 2017):

- 1 - 1000 micrometers: micro-fractures and lamination
- 0.05 - 1 micrometers: intergranular pores
- 10 - 50 nanometers: intragranular pores
- 5 - 10 nanometers: organic matter-hosted pores
- 2.8 - 5 nanometers: intra-clay platelet pores

Pore size distributions are very heterogenous within the Dean and Wolfcamp A samples. Conversely, the Wolfcamp B samples have a predominant distribution of pores less than 50 nm.

The middle Spraberry samples from MICP analyses has a relatively even distribution of pore throat diameters.

The permeability, effective tortuosity, and geometric tortuosity calculated from geometric means for various pore-throat network ranges are compiled in Table 4-8. The largest permeabilities and lowest tortuosities are observed in pore throat networks greater than 100 nm. The lowest permeabilities and highest tortuosities are observed in pore throat networks between 2.8 nm and 10 nm.

Table 4-6 Pore characteristics of samples

Sample ID	Bulk density (g/cm^3)	Skeletal density (g/cm^3)	Porosity (%)	Total pore area (m^2/g)	Total pore volume (mm^3/g)	Average pore-throat diameter (nm)
W537A SPRA	2.598	2.606	0.325	0.35	1.2	14.1
X340 WCa	2.654	2.664	0.371	0.52	1.4	10.7
X682 WCa	2.166	2.472	0.550	0.58	2.2	76.2
Y538 WCa	2.685	2.701	0.621	0.50	2.3	18.5
Y540 WCa	2.403	2.466	2.556	6.69	10.6	6.4
Y782 WCb	2.042	2.225	8.260	23.35	40.5	6.9
Y863 WCb	2.252	2.521	10.644	15.69	47.3	12.1
Z200 Dean	2.528	2.660	4.956	5.07	19.6	15.5
Z281 Dean	2.549	2.626	2.953	4.84	11.6	9.6
Z293 Dean	2.484	2.648	6.194	1.31	24.9	75.9
Z823 WCb	2.208	2.527	12.638	12.37	57.3	18.5

Table 4-7 Pore size distributions of samples

Sample ID	Pore-throat diameter %								
	10-1275μm	10-100μm	10-50μm	1-10μm	0.1-1μm	0.05-0.1μm	0.01-0.05μm	0.005-0.01μm	0.0028-0.005μm
W537A SPRA			24.5	23.1	10.3	4.50	14.2	6.87	16.4
X340 WCa			13.4	18.4	8.22	0.63	11.8	33.5	13.9
X682 WCa				5.22	4.97	2.29	3.25	28.8	45.6
Y538 WCa			12.1	34.2	9.10	1.11	13.4	22.1	7.95
Y540 WCa			7.29	6.94	4.17	2.50	18.2	29.2	31.7
Y782 WCb	3.90	8.42		4.15	2.03	1.22	12.8	52.2	15.3
Y863 WCb	13.0	9.39		2.29	1.57	1.46	47.8	22.3	2.18
Z200 Dean			1.32	3.35	3.06	11.0	67.9	10.8	2.61
Z281 Dean			0.05	1.85	1.60	2.14	61.1	28.9	4.29
Z293 Dean			1.34	2.67	81.2	10.8	1.05	2.27	0.67
Z823 WCb	10.0	1.56		1.13	3.52	25.5	51.8	5.41	1.11

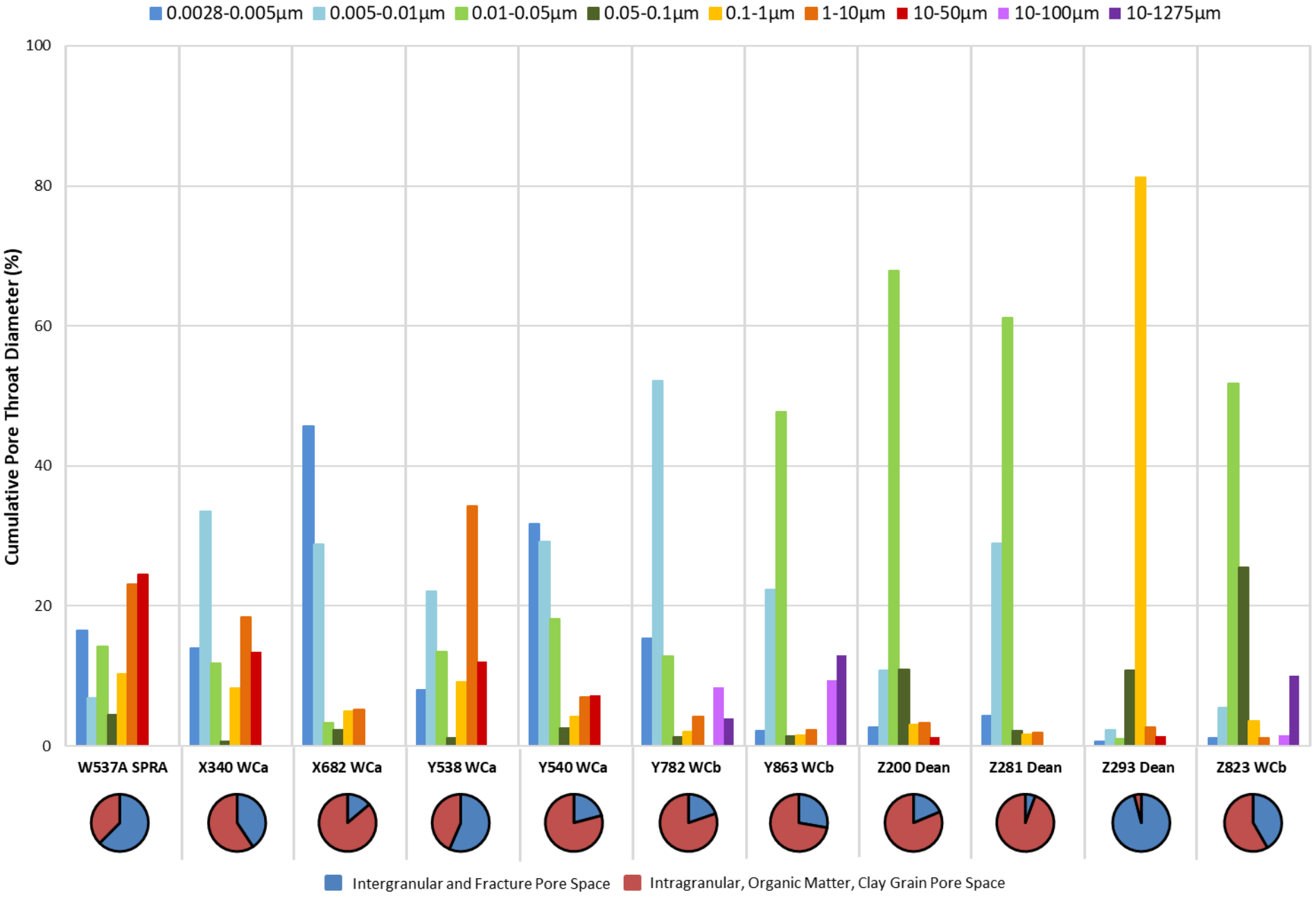

Figure 4-7 Pore size distributions of samples

Table 4-8 Comparison of permeabilities and tortuosities (geometric mean) associated with various pore throat

	2.8-10 nm pore-throat network				2.8-50 nm pore-throat network				>100 nm pore-throat network			
Sample ID	Pore-throat volume (%)	Permeability (nD)	Effective Tortuosity D_0/D_e	Geometrical Tortuosity L_e/L	Pore-throat volume (%)	Permeability (nD)	Effective Tortuosity D_0/D_e	Geometrical Tortuosity L_e/L	Pore-throat volume (%)	Permeability (nD)	Effective Tortuosity D_0/D_e	Geometrical Tortuosity L_e/L
W537A SPRA	23.3	0.242	7.93E+03	5.07	37.5	0.449	5.82E+03	4.35	58.0	3.21E+05	6.88	0.15
X340 WCa	47.5	0.566	3.80E+03	3.75	59.3	1.205	2.60E+03	3.10	40.1	1.40E+05	7.62	0.17
X682 WCa	74.4	0.828	9.07E+05	70.6	77.7	0.967	8.39E+05	67.9	10.2	7.27E+06	306	1.30
Y538 WCa	30.1	1.038	4.23E+03	5.12	43.5	3.093	2.45E+03	3.90	55.4	4.87E+05	6.17	0.20
Y540 WCa	60.9	2.004	3.06E+03	8.84	79.1	6.437	1.71E+03	6.60	18.4	1.05E+04	42.2	1.04
Y782 WCb	67.5	15.81	2.65E+04	46.8	80.3	24.26	2.14E+04	42.0	18.5	2.23E+07	22.3	1.28
Y863 WCb	24.5	68.59	2.73E+04	53.9	72.3	94.18	2.33E+04	49.8	26.3	9.35E+08	7.40	0.57
Z200 Dean	13.4	21.06	7.54E+02	6.11	81.3	60.50	4.45E+02	4.70	7.73	3.98E+03	54.9	1.65
Z281 Dean	33.2	5.088	4.06E+02	3.46	94.4	15.65	2.32E+02	2.62	3.50	1.10E+02	87.4	1.61
Z293 Dean	2.94	75.11	4.38E+02	5.21	3.99	72.29	4.46E+02	5.26	85.2	5.51E+02	162	3.16
Z823 WCb	6.53	71.89	2.40E+04	55.1	58.3	819.7	7.10E+03	30.0	16.3	2.76E+08	12.2	0.61

4-6 Production Data

Monthly production data for all wells were obtained from Drilling Info. Production curves for the wells are presented in Figure 4-8. Production in the wells began as early as December 2011 in Well Z and began as late as April 2015 in the Well Y. Two distinct production behaviors are observed in the wells. Well W and Well X exhibit peak oil and gas production with the first four months of initial production and then immediately experience sharp production declines of 50% and 85% within two to seven months, respectively. Well Y and Well Z behave similarly to Well W and Well X, however, they experience a second round of increased production followed by rapid decline rates.

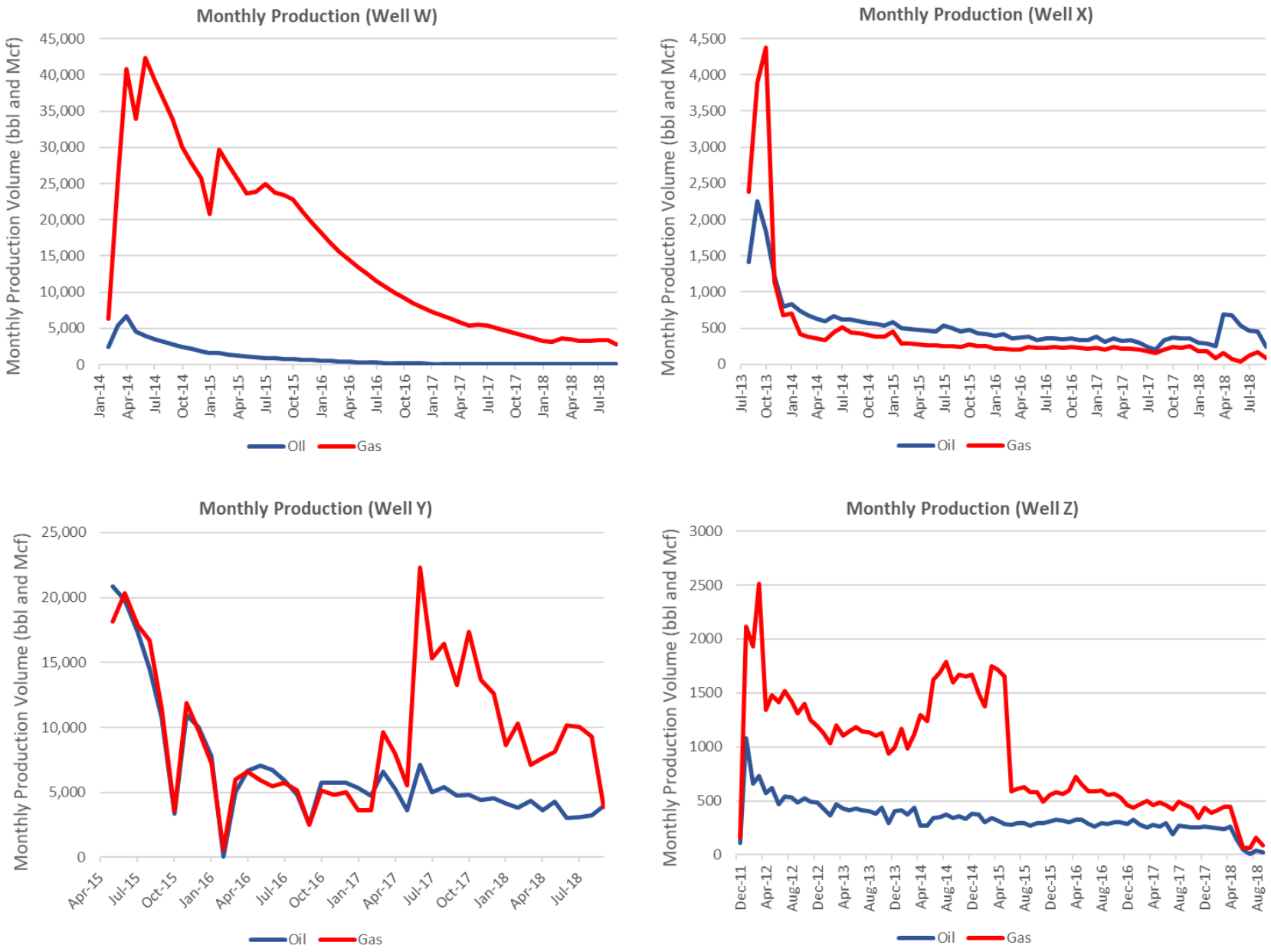

Figure 4-8 Monthly production curves of study wells

Chapter 5 - Discussion

5-1 Pore Structure vs. Mineralogy

No relationships are observed between pore structure and mineralogy. In Figure 5-2, the pore size distributions of two carbonate samples with similar mineralogical composition as well as two predominantly silicate samples with similar mineralogical composition are compared. Despite having very similar mineralogical compositions, the two sets of samples have very different pore-throat size distributions

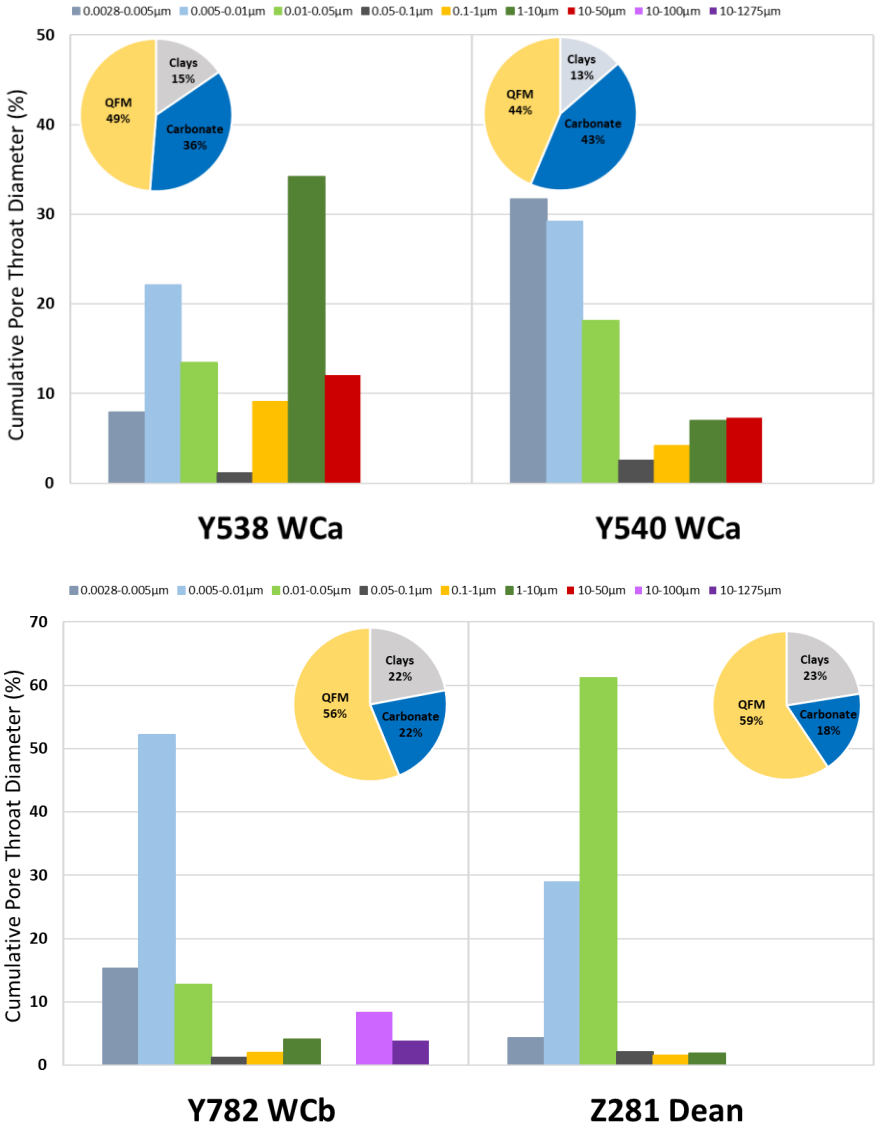

Figure 5-1 Comparison of two sets of samples with very similar mineralogical composition

5-2 Mineralogy vs. Organic Geochemistry

A relationship between clay content and TOC is observed in the samples. For samples with high TOC contents (>1%) and low clay contents (<20%), there is a strong positive correlation between clay content and TOC (Figure 5-3). This finding was also observed by Kulia et al. (2012) who found a strong positive correlation between clay content and TOC in samples with high organic content and low clay content. A relationship between TOC and other mineral compositions is not observed in the samples.

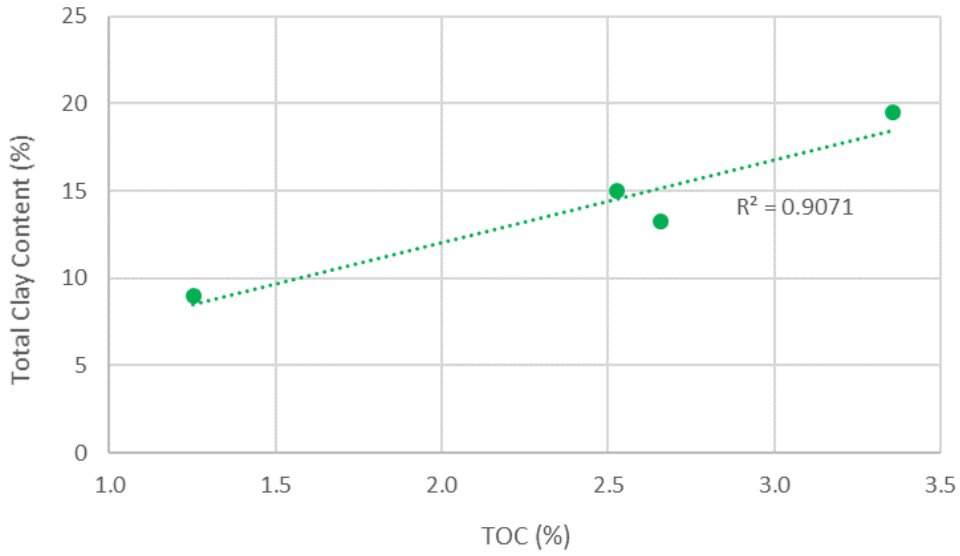

Figure 5-2 Comparison of clay content and TOC

5-3 Pore Structure vs. Organic Geochemistry

Relationships between the pore structure and organic geochemistry are observed within the sample set. As the kerogen is converted to hydrocarbons, pores are generated in the kerogen as the space once occupied by kerogen enters a new phase. Consequently, S1 values, the measurement of the free hydrocarbons present in the sample before analysis, are a good indication of the thermal maturity of samples. S1 values and porosities obtained from MICP analyses for several samples are compared in Figure 5-3. A positive correlation is observed between the S1 values and porosities of samples collected from the Wolfcamp B, Wolfcamp A, and Spraberry Formations. A relationship was not observed between the S1 values and porosities of samples collected from the Dean Formation as samples from the Dean Formation had relatively large porosities and low S1 values. The S1 values and percentage of pores throats within the 5-50nm range were compared in samples from the Wolfcamp B, Wolfcamp A, and Spraberry Formations (Figure 5-3). A weak positive correlation is observed between S1 values and percentage of pores throats within the 5-50 nm range in these samples. These findings indicate that within the Wolfcamp and Spraberry Formations, the generation of pores associated with intragranular and organic matter is dependent on thermal maturation.

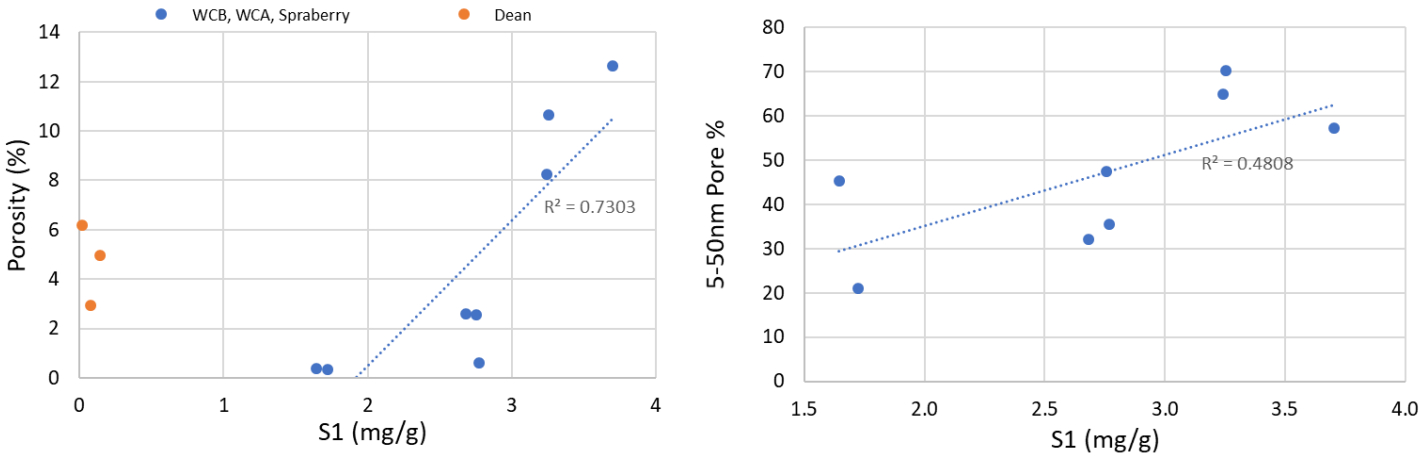

Figure 5-3 Comparisons of S1 values and porosity (left) and 5-50 nm pore throat percentage (right).

5-4 Pore Connectivity Characteristics

In samples which imbibition tests with DI and DT2 as wetting fluids were conducted, DT2 runs consistently have higher Stage 3 slopes than DI water runs. This indicates that the hydrophobic pore network is better connected than the hydrophilic pore network. Mineralogy also appears to influence pore connectivity in the sample set. A weak positive correlation exists between quartz content and pore connectivity in the hydrophobic pore networks of the samples (Figure 5-4). As quartz weight percentage increases, pore connectivity in the hydrophobic pore networks of the samples increases. No other relationships are observed between the mineralogy and the pore networks of the samples.

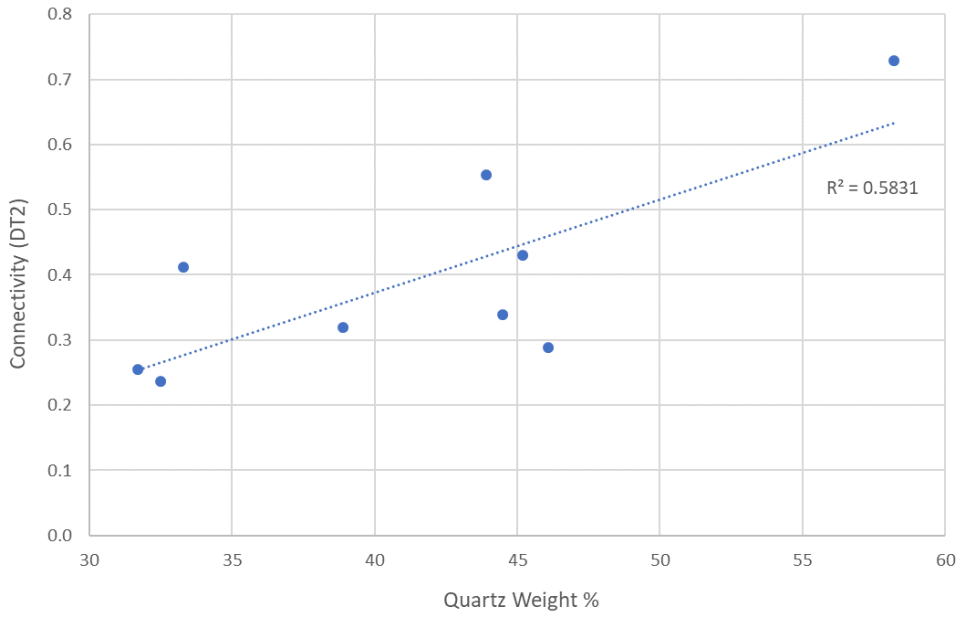

Figure 5-4 Comparison of quartz weight % and DT2 imbibition slopes

5-5 Porosity vs. Permeability

Geometric permeabilities for the following pore throat networks are indirectly obtained from MICP analysis: 2.8-10 nm, 2.8-50 nm, and greater than 100 nm. A representative permeability for each sample was then chosen based on the range of pore throat diameters that are most prevalent in the sample. The geometric permeabilities selected for each sample and the percentage of pores in the most prevalent pore throat network are presented in Table 5-1.

Table 5-1 Predominant pore throat network and associated geometric permeabilities

	Pore-throat size (nm)	Pore-throat volume (%)	k (nD)
W537A SPRA	>100	58.0	321065
X340 WCa	2.8-50	59.3	1.21
X682 WCa	2.8-10	74.4	0.828
Y538 WCa	>100	55.4	486906
Y540 WCa	2.8-50	79.1	2.00
Y782 WCb	2.8-50	80.3	15.8
Y863 WCb	2.8-50	72.3	68.6
Z200 Dean	2.8-50	81.3	21.1
Z281 Dean	2.8-50	94.4	5.09
Z293 Dean	>100	85.2	551
Z823 WCb	2.8-50	58.3	71.9

The relationship between the porosities and representative geometric permeabilities of samples which have a predominant pore throat network of either 2.8-10 nm or 2.8-50 nm is examined in Figure 5-5. A strong positive correlation is observed between the porosities and matrix permeabilities of these samples. This indicates that pore connectivity in the 2.8-10 nm and 2.8-50 nm range in samples with larger porosities is fairly high. This finding is generally in agreement with results from spontaneous fluid imbibition experiments. The MICP porosities of samples and estimated permeabilities from samples which have high imbibition connectivity

slopes are examined in Figure 5-5. A positive correlation is also observed between the porosities and estimated permeabilities of these samples.

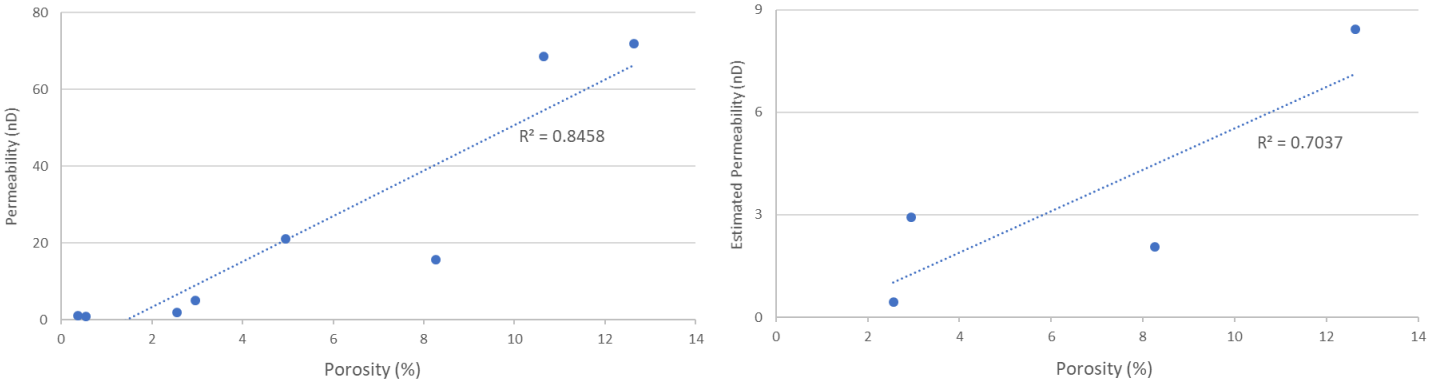

Figure 5-5 Comparison of porosity and representative geometric permeabilities from MICP (Left). Permeabilities estimated from imbibition tests (Right).

5-6 Permeability and Pore Structure

Samples which have a predominant network of pores larger than 100 nm have significantly higher permeabilities and lower tortuosities than samples whose predominant pore throat network ranges from 2.8-10 nm and 2.8-50 nm. Samples which have a predominant pore throat network of 2.8-10 nm exhibit the lowest permeabilities and highest tortuosities. Permeabilities in samples with predominantly larger than 100 nm pores are as high as five orders of magnitudes larger than permeabilities in samples with predominantly 2.8-10 nm pores. Tortuosities in samples with predominantly 2.8-10 nm pores are 22-472 times greater than tortuosities in samples with predominantly larger than 100 nm pores. These results indicate that pore size distribution is a significant controlling factor on permeability and the significant presence of pores with diameters between 2.8-50 nm range inhibits fluid flow.

Chapter 6 – Conclusions

6-1 Conclusion

Samples from the Wolfcamp B, Wolfcamp A, Dean, and Spraberry Formations were investigated with a suite of experiments to develop a better understanding of the pore structure and fluid migration within these formations. Conclusions from the study are as follows:

- The majority of samples exhibit a significant pore size distribution in pore throat diameter ranges associated with intra-clay grain space, organic matter hosted pores, and intragranular pores.
- A positive correlation is observed between the S1 values and pore structure of several samples. The results indicate that thermal maturation plays a significant role in the generation of pores with diameters between 5-50nm. These pores contribute as much 90% of the overall porosity in some samples.
- The hydrophobic pore networks of the samples are better connected than the hydrophilic pore networks of the samples.
- A strong positive correlation is observed between the permeabilities and porosities of samples indicating that samples with higher porosities exhibit high pore connectivity.
- Pore size distribution is found to be a significant controlling factor on permeability. Samples with a predominant presence of pores with diameters between 2.8-50 nm have significantly lower permeabilities and higher tortuosities than samples which have a predominant network of pores larger than 100 nm.

6-2 Recommendations

A significantly larger data set must be acquired in order to validate the interpretations from this study. More samples from additional depths in the study wells also need to be acquired as unconventional reservoirs are inherently very anisotropic. Additionally, samples should be investigated with a wider suite of methods such as nitrogen physisorption and field emission-scanning electron microscopy in order to further understand pore structure and particle size distribution.

References

Ball, M.M. 1995. Permian Basin province. U.S. Geological Survey 044. pp.1-21.

Barber, T. 2014. Applying vacuum saturation to study the pore structure of tight shales. Geological Society of America Annual Meeting. Vancouver, BC

Bureau of Economic Geology (BEG). 2008. Permian Basin geologic synthesis project: project GIS data. Austin, Texas.

Business Wire. 2017. Game-changing new research on prolific Permian Basin estimates 60 billion to 70 billion barrels remain, IHS Markit Says. www.businesswire.com/news/home/20170925005181/en/game-changing-new-research-prolific-permian-basin-estimates.

DrillingInfo, 2019. www.drillinginfo.com

Engle, M., and R. Reyes. 2016. Geochemistry of formation waters from the Wolfcamp and Cline shales: Insights into brine origin, reservoir connectivity, and fluid flow in the Permian Basin, USA. Chemical Geology. 425. 10.1016/j.chemgeo.2016.01.025.

Flint, A.L., and L.E Flint. 2002. 2.2 Particle density. In: Methods of soil analysis: Part 4. Physical methods. Soil Science Society of America. pp. 229–240.

Gamero-Diaz, H., C.K. Miller, and R. Lewis. 2013. sCore: A mineralogy-based classification scheme for organic mudstones. SPE Annual Technical Conference and Exhibition, Presentation at the Society of Petroleum Engineers, New Orleans, LA,

USA.10.2118/166284-MS.

Gao, Z.Y., Q.H. Hu, and H.C. Liang. 2013. Gas diffusivity in porous media: Determination by mercury intrusion porosimetry and correlation to porosity and permeability. Journal of Porous Media, 16(7): 607-617

Gao, Z., and Q.H. Hu. 2012. Using spontaneous water imbibition to measure the effective permeability of building materials. Special Topics and Reviews in Porous Media – An International Journal, 3 (3): 209-213.

Hamlin, H.S., and R.W. Baumgardner. 2012. Wolfberry (Wolfcampian-Leonardian) deep-water depositional systems in the Midland Basin: Stratigraphy, lithofacies, reservoirs, and source rocks. Austin, Texas: Bureau of Economic Geology, University of Texas at Austin. Print.

Handford, C. R. 1981. Sedimentology and genetic stratigraphy of Dean and Spraberry Formations (Permian), Midland Basin, Texas. American Association of Petroleum Geologists Bulletin, vol. 65, no. 9, pp. 1602–1616.

Hills, J.M. 1972. Late Paleozoic sedimentation in west Texas Permian Basin. American Association of Petroleum Geologists Bulletin, vol. 56, no. 12, pp. 2303–2322.

Hills, J.M. 1984. Sedimentation, tectonism, and hydrocarbon generation in Delaware Basin, west Texas and southeastern New Mexico. American Association of Petroleum Geologists Bulletin, vol. 68, no. 3, pp.250–267.

Hu, Q.H., Y. Zhang, X. Meng, and Z. Li. Characterization of micro-nano pore networks in shale oil reservoirs of Paleogene Shahejie Formation in Dongying Sag of Bohai Bay Basin, East China. Petroleum Exploration and Development, vol. 44, no. 5, 2017, pp. 720–730

Hu, Q.H., P. Persoff, and J.S. Wang. 2001. Laboratory measurement of water imbibition into low-permeability welded tuff. Journal of Hydrology, vol.242, pp.64-78.

Hu, Q.H., R. P. Ewing, and S. Dultz. 2012. Low pore connectivity in natural rock. Journal of Contaminant Hydrology, vol.133, pp.76-83.

Hu, Q.H., R. P. Ewing, and H. Rowe. 2015. Low nanopore connectivity limits gas production in Barnett Formation. Journal of Geophysical Research: Solid Earth, vol. 120, no. 12, pp. 8073–8087., doi:10.1002/2015jb012103.

Hu, Q.H., and R.P. Ewing. 2014. Integrated experimental and modeling approaches to studying the fracture-matrix interaction in gas recovery from Barnett Shale. Report 09122-12, University of Texas at Arlington.

Hughes, J.D. 2018. Shale reality check: Drilling into the U.S. government's rosy projections for shale gas and tight oil production through 2050. Post Carbon Institute.

Katz, A.J., and A. H. Thompson. 1986. Quantitative Prediction of Permeability in Porous Rock. Physical Review B, vol. 34, no. 11, pp. 8179–8181.

Kuila, U., M. Prasad, A. Derkowski, and D.K. McCarty. 2012. Compositional controls on mudrock pore-size distribution: An example from Niobrara Formation. Society of Petroleum Engineers. doi:10.2118/160141-MS

Philip, J.R. 1957. The theory of infiltration: 4. Sorptivity and algebraic infiltration equations. Soil Science. vol.84, pp.257–265.

Porosimeter Autopore IV 9520. AGH University of Science and Technology.

Society for Sedimentary Geology (SEPM). 2013. A brief tectonic history of the Permian Basin. Permian Basin Tectonics. http://www.sepmstrata.org/page.aspx?pageid=137

Soreghan, G.S., and M.J. Soreghan. 2013. Tracing clastic delivery to the Permian Delaware Basin, USA: Implications for paleogeography and circulation in westernmost equatorial Pangea. Journal of Sedimentary Research, v. 83, p. 786-802.

U.S Energy Information Administration (EIA). 2014. Six formations are responsible for surge in Permian Basin crude oil production. Today in Energy. https://www.eia.gov/todayinenergy/detail.php?id=17031

U.S Energy Information Administration. 2017. Permian Basin Wolfcamp shale play geology review. https://www.eia.gov/maps/pdf/PermianBasin_Wolfcamp_EIAReport_Oct2018

Wang, S., F. Javadpour, and Q.H. Feng. 2016. Confinement correction to mercury intrusion capillary pressure of shale nanopores. Scientific Reports, 6: 20160, doi:10.1038/srep20160.

Washburn, E.W. 1921. Note on a method of determining the distribution of pore sizes in a porous material, Proceedings of the National Academy of Sciences of the United States of America, vol. 7, pp. 115–116.

Appendix A

Methods and Procedures for Geochemical Analysis at Weatherford Laboratories

Rock Sample Preparation

Samples for Total Organic Carbon (TOC) and/or Programmed Pyrolysis may each require varying levels of sample preparation. Groups of samples are evaluated as to their respective condition as received and are handled differently depending on the various types of contaminants, lithologies, and analytical objectives. Samples are not high-graded prior to grinding unless specifically instructed by the client. When necessary and as instructed, water washing may be required to remove water-based mud. Solvent washing can be utilized to remove oil-based and/or synthetic-based mud. Additional solvent extraction of the crushed rock will be necessary to completely remove the contaminating oil-based and/or synthetic-based mud. Sample picking may also be necessary to remove lost circulation material or known cavings. Samples for TOC and Programed Pyrolysis are then ground to pass through a fine mesh sieve prior to analysis.

Total Organic Carbon

Approximately 0.10 g of crushed rock is accurately weighed and then digested with concentrated hydrochloric acid to remove all carbonates from the sample. At this point, gravimetric carbonate content can be determined if requested. Following digestion, the sample is washed through a filtering apparatus, placed in a combustion crucible and dried. After drying, the sample is analyzed with a LECO Carbon Analyzer with detection limits to 0.01 weight

percent. Standards and sample duplicates are tested regularly to assure superior instrument performance.

Programmed Pyrolysis (Rock-Eval II, Rock-Eval VI, Source Rock Analyzer)

Programmed pyrolysis (Rock-Eval and SRA) is performed to assess source rock quality and thermal maturity (e.g., Peters, 1986; Peters and Casa, 1994). In programmed pyrolysis, crushed rock samples are heated in an inert environment to determine the yield of hydrocarbons and CO2. The sample is initially held isothermally at 300°C for 3 minutes, producing the S1 peak by vaporizing the free (unbound) hydrocarbons. High S1 values indicate either large amounts of kerogen-derived bitumen (as in an active source rock) or the presence of migrated hydrocarbons. The oven then increases in temperature by 25°C/minute to a final temperature of approximately 600°C, depending on the instrument type. During this time, hydrocarbons that evolve from the sample as a function of the pyrolytic degradation of the kerogen are measured, generating the S2 peak and is proportional to the amount of hydrogen-rich kerogen in the rock. The temperature at which the S2 peak reaches a maximum, "T_{max} ", is a measure of the source rock maturity. Accuracy of T max is 1-3°C, depending on the instrument, program rate and sample size, but can also vary by organic matter type. T_{max} values for samples with S2 peaks less than 0.2 mg HC/g rock are often inaccurate and should be rejected unless a definitive kerogen peak is noted from the pyrogram. Any carbon dioxide released between 300° and 390°C is also measured, generating the S3 peak, providing an assessment of the oxygen content of the rock. In addition to the standard programmed pyrolysis method, we have several additional methods available designed to provide the client with additional useful information as it relates to the geochemical nature and potential of a rock sample including but not limited to TOC

quantification, Carbonate quantification, Reservoir Oil Quality, APIR and Kerogen Kinetic analyses. A summary of analytical results from Programmed Pyrolysis follows.

S1: free oil content (mg hydrocarbons per gram of rock)

S2: remaining hydrocarbon potential (mg hydrocarbons per gram of rock)

S3: organic carbon dioxide (mg CO 2 per gram of rock)

TOC: total organic carbon content (wt. %)

T_{max}: temperature at maximum evolution of S2 hydrocarbons

Ratios: hydrogen index (HI), oxygen index (OI), production index (PI),

S2/S3, and S1/TOC

Vitrinite Reflectance and Visual Kerogen Assessment

Visual kerogen assessments complement chemical assessments by recording information from the discrete particles (macerals) that make up the sedimentary organic matter. Vitrinite macerals are particles of sedimentary organic matter derived from wood, and their reflectance of incident light under oil immersion is used to assess the thermal maturity of a sample. Vitrinite reflectance (%R o) increases with increased depth of burial (i.e., increased thermal exposure), and is an indication of the maximum temperature to which these particles have been exposed. The reflectance microscope measures the amount of reflected light relative to the incident light and expresses this ratio as a percentage. Vitrinite reflectance values range from about 0.25% (immature) to a high of about 5 or 6% (very mature). A population of vitrinite particles is found in almost all rock samples of Devonian or younger age (older samples pre-date the evolution of

land plants, the source of vitrinite). Selecting the appropriate vitrinite population for subsequent reflectance measurements is a somewhat subjective process. The in-situ population must be identified, and must exclude vitrinite derived from cavings and reworked organic matter. Reworked vitrinite that was redeposited in the sediments may have higher reflectance that will skew the measurements towards higher R o values if not recognized and removed from the average. In cuttings samples, cavings from overlying less mature sediments may skew the average towards lower values. Generally, when cavings are excluded, the lowest reflecting population is found to be indicative of the indigenous population, but this evaluation is made in combination with visual kerogen assessments, Rock-Eval Tmax measurements, and data for the extent of kerogen conversion.

Vitrinite reflectance values are divided into the following stages of thermal maturity:

Stage	*Reflectance Range*
Immature	0.2% to 0.6%
Oil window maturity	0.6% to 1.1%
Condensate or wet-gas window	1.1% to 1.4%
Dry gas window	1.40% plus

Thermal alteration indices (TAI) are determined from the color of organic matter when viewed under transmitted light through a strewn slide mount of kerogen. Lighter colored organic matter is indicative of low maturity, whereas darker material is indicative of higher thermal maturity.

Maceral composition is an assessment of the percentages of various organic particles found in kerogen samples. These particles are related to the oil and gas potential of the organic

matter and are generally described as amorphous, exinitic, vitrinitic, inertinitic, or solid bitumen percentages. The former two macerals are primarily oil-prone particulate matter, whereas vitrinitic particles are indicative of gas-prone organic matter. Inertinitic matter is very hydrogen-poor and has no potential for generation of commercial quantities of hydrocarbons. The presence of solid bitumen is indicative of in situ generated hydrocarbons, migrated hydrocarbons, or contamination. Other observations from visual kerogen assessment include the quality of the organic matter (oxidized, well preserved), and the presence of palynomorphs (which can reveal key aspects of the depositional environment).

Appendix B

Laboratory Methods and Procedures for TOC and Pyrolysis Analysis at GeoMark Research, LLC.

Procedures – GeoMark Research, LLC.

1. Sample Requirements for a Typical Geochemical Program

For geochemical analysis a teaspoon (ca. 10 g.) of sample material is needed when TOC, Rock-Eval, vitrinite reflectance and residual hydrocarbon fluid fingerprinting is to be completed. If possible, a tablespoon is preferred. However, it is possible to complete a detailed program with even less sample, although there is dependency on the sample characteristics (e.g., organic richness, abundance of vitrinite, amount of staining). Sample prep includes grinding the sample with mortar and pestle until it passes through a 60 mesh sieve.

2. Total Organic Carbon (TOC) – LECO C230 instrument

Leco TOC analysis requires decarbonation of the rock sample by treatment with hydrochloric acid (HCl). This is done by treating the samples with concentrated HCl for at least two hours. The samples are then rinsed with water and flushed through a filtration apparatus to remove the acid. The filter is then removed, placed into a LECO crucible and dried in a low temperature oven (110 ^{o}C) for a minimum of 4 hours. Samples may also be weighed after this process in order to obtain a % Carbonate value based on weight loss.

The LECO C230 instrument is calibrated with standards having known carbon contents. This is completed by combustion of these standards by heating to 1200 ^{o}C in the presence of oxygen. Both carbon monoxide and carbon dioxide are generated, and the carbon monoxide is converted

to carbon dioxide by a catalyst. The carbon dioxide is measured by an IR cell. Combustion of unknowns is then completed and the response of unknowns per mass unit is compared to that of the calibration standard, thereby the TOC is determined.

Standards are analyzed as unknowns every 10 samples to check the variation and calibration of the analysis. Random and selected reruns are done to verify the data. The acceptable standard deviation for TOC is 3% variation from established value.

3. Rock Eval / HAWK Pyrolysis

Approximately 100 milligrams of washed, ground (60 mesh) whole rock sample is analyzed in the Rock-Eval or HAWK instrument. Organic rich samples are analyzed at reduced weights whenever the S2 value exceeds 40.0 mg/g or TOC exceeds 7-8%. Samples must be re-analyzed at lower weights when these values are obtained at 100 mg.

RE-II Operating Conditions

S1: 300^{o}C for 3 minutes

S2: 300^{o}C to 550^{o}C at 25oC/min; hold at 550^{o}C for 1 minute

S3: trapped between 300 to 390^{o}C

RE-VI Operating Conditions

S1: 300^{o}C for 3 minutes

S2: 300^{o}C to 650^{o}C at 25^{o}C/min;

hold at 650^{o}C for 0 minute

S3: measured between 300 ^{o}C to 400 ^{o}C

HAWK Operating Conditions

S1: 300 ^{o}C for 3 minutes

S2: 300 ^{o}C to 650 ^{o}C at 25 ^{o}C /min;

hold at 650 ^{o}C for 0 minute

S3: measured between 300 ^{o}C to 400 ^{o}C

Measurements from Rock-Eval are:

S1: free oil content (mg HC/g rock)

S2: remaining generation potential (mg HC/g rock)

T_{max}: temperature at maximum evolution of S2 hydrocarbons (^{o}C)

S3: organic carbon dioxide yield (mg CO_2/ g rock)

Several useful ratios are also utilized from Rock-Eval and TOC data. These are:

Hydrogen Index (HI): S2/TOC x 100 (in mg HC/g TOC)

Oxygen Index (OI): S3/TOC x 100 (in mg CO_2/g TOC)

Normalized Oil Content: S1/TOC x 100 (in mg HC/g TOC)

S2/S3:

Production Index (PI): S1/ (S1+S2)

Instrument calibration is achieved using a rock standard. Its values were determined from a calibration curve to pure hydrocarbons of varying concentrations. This standard is analyzed every 10 samples as an unknown to check the instrument calibration. If the analysis of the standard ran as an unknown does not meet specifications, those preceding data are rejected, the instrument recalibrated, and the samples analyzed again. However, normal variations in the standard are used to adjust any variation in the calibration response. The standard deviation is considered acceptable under the following guidelines:

T_{max}: □ 2ºC

S1: 10% variation from established value

S2: 10% variation from established value

S3: 20% variation from established value

Analytical data are checked selectively and randomly. Selected and random checks are completed on approximately 10% of the samples. A standard is analyzed as an unknown every 10 samples.

4. Turnaround Time:

The standard turnaround time for sample orders over the past 12 months is approximately 2 to 3 weeks, depending on number of samples in the order.

Appendix C

Methods and Procedures of X-Ray Diffraction Analysis at Weatherford Laboratories

Bulk Sample Preparation

Spray Dry

A representative portion (6 grams minimum, preferably 10 grams) of each sample is selected for XRD analysis. Samples are disaggregated using mortar and pestle and portioned out for bulk and clay analyses. The bulk portion is ground into a slurry using a McCrone Micronizing Mill. The slurry is transferred to an air brush assembly and spray dried using a James Hutton Institute Spray Drying Oven. Randomly oriented spherical aggregates are then loaded into stainless steel sample holders. This method eliminates preferred orientation of minerals and allows for improved reproducibility of the bulk XRD patterns. [Sp. Ed. Bish, D. L. and Post, J. E. (1989); Hillier, S (2002b)].

Minimal Material

A representative portion (2 grams minimum) of each sample is selected for XRD analysis. Samples are hand ground in an agate mortar and pestle to a fine powder. A portion of each ground sample is loaded into a stainless steel sample holder, modified to accommodate a side loading method. This side loading method allows the sample to be sifted and promotes a random particle orientation, minimizing preferred orientation.

Bulk/Whole Rock Analysis

These bulk sample mounts are scanned with a Bruker AXS D4 Endeavor X-ray diffractometer using copper K-alpha radiation. To eliminate K-beta peaks and reduce

background noise, nickel filter slits and air scatter screens are utilized, respectively. The scanning parameters for a bulk scan are from 5° 2θ to 70° 2θ at a step size of 0.02° per step. Full scanning parameters are defined below (for both bulk and clay):

- Operating voltage: 50Kv
- Operating amperage: 40mA
- Axial soller slit is in place
- Goniometer diameter: 400mm
- Lynx Eye High speed detector with a 2θ scanning range of 4°
- A nickel filter for K beta peaks
- An air scatter screen to reduce fluorescence
- Variable divergent slit at 0.3mm for bulk and 0.5mm for clay

Bulk Mineral Quantification

MDI Jade TM 9+ software and ICDD PDF 4+ 2015 database, with over 790,000 known compounds, are used to identify mineral phases present in the bulk diffractograms. Reference Intensity Ratio (RIR) method is used to quantify the whole rock. The RIRs (e.g., Mineral Intensity Factors (MIF)) are generated for each diffractometer using pure mineral standards mixed with quartz. The primary peaks of the minerals present are measured using the area under the curve to one standard deviation (subtracting the background). When an uncommon mineral that is not in our RIR library and pure mineral standards are not available, whole pattern fitting with Rietveld refinement is applied.

X-ray diffraction cannot identify non-crystalline (amorphous) material, such as organic material and volcanic glass. However, samples containing a large amount of amorphous material show an anomalous “hump” in the XRD pattern. If further evaluations are required, Bruker AXS TOPAS v4.2 software is used to provide an estimate of the amount of amorphous material. Scans undergo full-pattern-fitting and Rietveld refinement using structure phase files previously identified by Jade and ICDD software (see above).

Clay Sample Preparation

An oriented clay fraction mount is prepared for each sample from hand ground powder. The samples are treated with a small amount of sodium hexametaphosphate as a deflocculant mixed with distilled water. The samples are then physically dispersed using a Fisher Scientific Ultra Sonifier to bring the clays into suspension. The samples are sized fractionated by centrifuging. After centrifuging, the supernatant containing the less than 2 micron clay fraction is vacuumed through a filter membrane glass tube that collects the solids on to a millipore filter.

These oriented solids are mounted on glass slides producing highly uniform diffraction mounts [Drever, 1973]. The glass slides are loaded into desiccant bowls containing 99.9% ethylene glycol for an extended period of time at a temperature of 110°C. The samples are loaded directly from the desiccant bowl to ensure maximum sample glycolation. The glycolated clays are also scanned in a Bruker AXS diffractometer using the following scan parameters: 2° 2θ to 30° 2θ at a step size of 0.02° per step. After the glycolated slide is scanned, the slides are heat-treated in a furnace at 375°C for one hour and rescanned at the same clay parameters stated above. This process aids in identifying the expandable, water-sensitive minerals. When samples contain high levels of carbonates combined with low clay quantities, we may need to return to

the sample and remove the carbonates to obtain a better clay scan for accurate identification and quantification.

Clay Mineral Identification and Quantification

Mixed-layer clays, particularly illite/smectite (I/S) are identified following the multiple peak method of Moore and Reynolds (1997). This entails measuring the 001/002 and 002/003 peaks of the illite/smectite. NEWMOD clay mineral generation program is used to create theoretical clay patterns, clay mixtures, and illite crystallinity. Identification of the amount of smectite (percent expandability) is also verified using the heat treated diffractogram overlain on the glycolated diffractogram in MDI Jade.

Kaolinite and chlorite are identified by the relative proportions of the peaks at 3.59 Å (kaolinite 002) and 3.54 Å (chlorite 004).

Clay mineral quantification includes: (1) the actual amount of discrete clay mineral species in the sample, and (2) the "expandability" or amount of smectite in mixed-layer clays, if present. Illite/Smectite (I/S) is the most common mixed-layer clay, but there are also chlorite/smectite (corrensite) and kaolinite/smectite. There are several tables in Moore and Reynolds (1997) that list 2θ positions and their correlative percent smectite in I/S (Table 8.3, p. 273) or C/S (Table 8.4, p.281).

The Mineral Intensity Factor (MIF) method of Moore and Reynolds (1997) is applied to quantify the clay species. Weatherford has calculated MIFs for most clay minerals encountered. The area of the specific mineral peak being used is divided by the MIF in the quantification process. The clay species is normalized to the total clay value derived from the bulk analysis.